



HAL
open science

Development of a Large-Eddy Simulation Methodology for the Analysis of Cycle-to-Cycle Combustion Variability of a Lean Burn Engine

O. Benoit, K. Truffin, S. Jay, J. van Oijen, Y. Drouvin, T. Kayashima, P.
Adomeit, C. Angelberger

► **To cite this version:**

O. Benoit, K. Truffin, S. Jay, J. van Oijen, Y. Drouvin, et al.. Development of a Large-Eddy Simulation Methodology for the Analysis of Cycle-to-Cycle Combustion Variability of a Lean Burn Engine. *Flow, Turbulence and Combustion*, 2022, 108 (2), pp.559-598. 10.1007/s10494-021-00278-7 . hal-03693904

HAL Id: hal-03693904

<https://ifp.hal.science/hal-03693904>

Submitted on 13 Jun 2022

HAL is a multi-disciplinary open access archive for the deposit and dissemination of scientific research documents, whether they are published or not. The documents may come from teaching and research institutions in France or abroad, or from public or private research centers.

L'archive ouverte pluridisciplinaire **HAL**, est destinée au dépôt et à la diffusion de documents scientifiques de niveau recherche, publiés ou non, émanant des établissements d'enseignement et de recherche français ou étrangers, des laboratoires publics ou privés.

Development of a Large-Eddy Simulation methodology for the analysis of cycle-to-cycle combustion variability of a lean burn engine

O. Benoit^{*},¹, K. Truffin², S. Jay², J. van Oijen³, Y. Drouvin¹, T. Kayashima⁴, P. Adomeit⁵, C. Angelberger²

¹ TOYOTA GAZOO Racing Europe GmbH, Chassis & Powertrain Development, Toyota Allee 7, 50858 Köln, Germany

² IFP Energies Nouvelles, 1 et 4 avenue de Bois-Préau, 92852 Rueil-Malmaison, France ; Institut Carnot IFPEN Transports Energie

³ Eindhoven University of Technology, Groene Loper 3, 5612 AE Eindhoven, Netherlands

⁴ Toyota Motor Corporation, Vehicle Development Center, 1 Toyota-Cho, 471-8571 Toyota City, Japan

⁵ FEV Europe GmbH, Neuenhofstraße 181, 52078 Aachen, Germany

(*) corresponding author: olivier.benoit@tgr-europe.com

Keywords: Large-Eddy Simulation, Lean Burn Combustion, Stretched Flamelet, Markstein Number, Coherent flame model

1 ABSTRACT

Ultra-lean burn conditions ($\lambda > 1.8$) is seen as a way for improving efficiency and reducing emissions of spark-ignition engines. It raises fundamental issues in terms of combustion physics and its modeling, among which the significant reduction of the laminar flame speeds and increase of the laminar flame thickness, as well as an increased sensitivity to local fuel/air equivalence ratio variations are essential to be accounted for as compared to conventional stoichiometric mixture conditions. In particular, the effects of the modified laminar flame characteristics on flame stretch during the early flame development in a spark ignited gasoline engine can be expected to become of importance. In the present work, a Large-Eddy Simulation combustion approach is presented and applied to the study of the cycle-to-cycle combustion variations of a direct injection gasoline engine operating both in stoichiometric and ultra-lean burn conditions. The Coherent Flame Model (CFM) approach is used and enriched via a correlation for the laminar flame velocity accounting for nonlinear stretch effects. The stretched flame calculations are validated against experimental results. Then, different engine operating points are computed in stoichiometric and ultra-lean burn conditions assessing the capacity of the approach to reproduce variations of combustion regimes. The results are analyzed in terms of cycle-to-cycle combustion variabilities (CCV) and the influence of the spark-plug orientation is studied. Finally, a detailed analysis of the flame development is presented with a particular emphasis on the analysis of the initial flame kernel development accounting for stretch effects in lean conditions and the analysis of extreme cycles in lean burn. A strong reduction of the flame velocity by one third was observed for lean-burn conditions due to non-linear stretch effects occurring during the early stage of the flame development while almost no change was observed for stoichiometric conditions. Moreover, the proposed approach was capable of handling the various conditions featuring significantly different combustion regimes (one order of magnitude for the Karlovitz number) with only a minor change in the model parameterization.

1 INTRODUCTION

In the context of global warming and intense research to reduce emissions and increase efficiency in light-duty vehicles (including passenger cars), major challenges are being faced by car manufacturers in order to meet environmental and societal expectations while maintaining sustainable private means of transportation. To this aim, several new technologies with lower local emission impacts have already arrived on the market: Hybrid Electrical Vehicles (HEV), Plug-in Hybrid Vehicles (PHEV), Battery Electric Vehicles (BEV), and in a lesser proportion Fuel Cell Electric Vehicles (FCEV). Worldwide projections in favor of sustainable development stipulate that conventional cars will still represent more than 50 percent of all car power units in service in the next three decades. Even though PHEV,

BEV and FCEV sales continuously increase, it is necessary to have a drastic reduction on car emissions for powertrains of the next decade. In parallel, the demand for fossil energy consumption will continue to grow as second and third world will continue to develop and with a limited access to electricity resource for mobility purposes [1]. Consequently, there is an increased interest of the automotive industry to develop high efficiency, low emission lean burn combustion units in the next decade, that could be used for both pure internal combustion engine (ICE) based and electrified powertrain types i.e. HEV, PHEV permitting to reach the ambitious goals on emissions reduction in the field of ground transportation with a presumable impact on the emissions for the next three decades. For this purpose, the use of computational fluid dynamics high-fidelity modeling tools can help to understand the interactions between the multiple physical phenomena involved and make relevant choices during the

engine design before testing. Up to now, the Reynolds-Averaged Navier-Stokes (RANS) method has been widely used for the calculation of internal flows in ICE. The whole turbulence spectrum is statistically modelled and the approach implicitly assumes the existence of a mean flow. In the case of ICE, this is usually understood as a mean cycle, the existence of which is not guaranteed.

In Large-Eddy Simulation (LES), the “mean cycle’s hypothesis” does not hold as only a part of the turbulence spectrum is modelled; the large fluctuating eddies contributing to the flow variability are resolved, while the smallest eddies are assumed to be more universal and are modelled. LES is more adapted to the representation of shear flows, such as the tumble in-flow encountered in ICE engine and generated between the valves and the valves seats during the intake process. Additionally, the eddy viscosity in LES is usually two orders of magnitude lower than in RANS, allowing the description of small-scale phenomena of interest, in particular the development of the early flame kernel.

In the last decade several research groups have conducted modeling studies and have assessed the capacity of LES to predict complex phenomena occurring in ICE and more particularly for the study of knock prediction [2-4] or cycle to cycle variations in spark-ignition engines [5-11]. More recently, attention has been paid to the description of the early flame kernel development and its interaction with turbulence which is of crucial importance because cycle-to-cycle variations (CCV) mostly find their origins during the early stage of ignition as explained in [12]. Such DNS analysis have helped to understand the intrinsic mechanisms of flame/turbulence interactions occurring in engine conditions. LES studies have been used to explore more complex combustion processes occurring when nearly stoichiometric or lean conditions are operated [13,14]. Nevertheless, none of these recent studies has pushed the engine simulation to the limits of flammability for real operating conditions with complex moving geometries, direct injection and complex ignition systems modeling. The present study is focused on the early flame kernel development and on the modeling elements to be included for the description of turbulence effects during this process. An appropriate description of this ignition stage is expected to strongly determine the accuracy of the prediction of the cycle-to-cycle variations in very lean conditions. The paper addresses this modeling issue and its consequences for practical applications thanks to available measurements on a direct injection spark-ignition single-cylinder engine with complex geometrical features. Moreover the use of LES can bring many details to help analyze the behavior of coupled turbulence-chemistry phenomena [15] occurring in lean burn conditions. The present work also aims at illustrating that LES should not only be seen as a tool providing just information on cycle-to-cycle variations or unwanted knocking events [4] but a more accurate representation of the intricate phenomena involved.

To take full advantage of lean combustion without deteriorating the engine stability one needs to account for a finer representation of the turbulent flow structures that may be second order when engines are operated at near stoichiometric conditions. At high air-fuel equivalence ratio conditions, laminar flame speeds are indeed very low and the influence of the flame curvature on the flame propagation needs to be considered in particular at the onset of ignition where curvatures are at their highest levels. While the former is usually taken into account in the solvers used in industry, the latter is a phenomenon that has been largely neglected up-to-now except in a few

fundamental studies on flame ignition [9,12]. The effect of the spark plug orientation on early flame kernel development and cycle-to-cycle variability has been studied in [16] in stoichiometric to rich conditions. To the authors’ knowledge, its effect at high air-fuel equivalence ratios has not been investigated in LES so far. Laminar flame speeds of planar and stretched (curved) flames can be analyzed in the framework of steady flamelet modelling which main idea is the decoupling of fast processes (chemical reaction) and slow processes (flame propagation). Under such conditions, LES presents a real advantage in terms of representation of the complex interactions between the flow non-stationarity and the chemistry. The proposed approach consists in implementing stretch effects on turbulent flames in a LES based approach using a priori calculations of 1D stationary stretched and un-stretched flames features.

The paper is organized as follows. This introduction is followed by Section 2 describing the equations of the coupled models ISSIM-LES/ ECFM-LES that are used in the simulations. Section 3 introduces how the laminar flame speeds and Markstein length scales are estimated for the engine conditions that are computed. The different computed cases are presented in Section 4. Section 5 describes the numerical set-up used for LES, the methodology and some basic validation of the accuracy of the simulations. Section 6 presents detailed analysis of the flame development with a particular emphasis on: 1) The analysis of the initial flame kernel development accounting for stretch effect in lean conditions, 2) The analysis of the cycle-to-cycle variations as compared to experimental results, 3) The analysis of extreme cycles in lean burn. Finally, the paper is summarized and concluded.

2 COMBUSTION MODELLING

2.1 Flame propagation modelling

We consider the ECFM-LES combustion model, which is based on the flame surface density (FSD) approach developed for LES of premixed turbulent flames.

In the chosen flamelet approach, combustion reactions occur in very fine zones that are much smaller than the LES mesh size. The filtering technique associated with the LES makes it possible to increase the size of these zones to a size comparable to that of a typical cell size Δ_x . However, with the finite volume approach, the flame front cannot be solved on a mesh because the gradients of the filtered quantities would be too large and would make the calculation numerically unstable. In practice, the fronts must be solved on a minimum number of grid points n_{res} ranging between 5 and 10 depending on the numerical scheme and on the combustion model. For this reason, the flame surface density must be filtered not on the scale Δ_x , but on a larger scale $\widehat{\Delta} = n_{res} \Delta_x$. To do so, implicit filtering is performed based on the mesh size and the unresolved transport. The unresolved transport term is closed under gradient assumptions and is written as a turbulent diffusion term.

In this formalism, the mixture composition is computed solving transport equations for the filtered mass density species $\widehat{\rho Y}_i$ (Fuel, O₂, CO₂, H₂O, CO, H₂ and N₂),

$$\begin{aligned} & \frac{\partial \bar{\rho} \tilde{Y}}{\partial t} + \underbrace{\nabla \cdot (\bar{\rho} \tilde{\mathbf{u}} \tilde{Y})}_{convection} \\ &= \underbrace{\nabla \cdot \left(\bar{\rho} \left(\frac{v}{S_c} + \frac{\hat{v}_t}{S_{c_t}} \right) \nabla \bar{\rho} \tilde{Y} \right)}_{diffusion} + \underbrace{\bar{\rho} \tilde{\omega}_Y}_{prod}, \end{aligned} \quad 1$$

Accentuations $\bar{\cdot}$ and $\tilde{\cdot}$ denote Reynolds filter and Favre filter respectively. $\tilde{\mathbf{u}}$ is the Favre filtered velocity vector. ν is the molecular kinematic viscosity and \hat{v}_t the subgrid scale kinematic viscosity estimated at scale $\widehat{\Delta}$.

$$\hat{v}_t = \nu_t \left(\frac{\widehat{\Delta}}{\Delta_x} \right)^{4/3} \quad 2$$

ν_t is the subgrid scale turbulent viscosity modeled using the Sigma model [17].

S_c and S_{c_t} are the laminar and turbulent Schmidt numbers, $\tilde{\mathbf{u}}$ the resolved flow field, and $\tilde{\omega}_Y$ the filtered reaction rate. The fuel density is also decomposed into unburned (“u”) and burned gases (“b”), so that transport equations similar to that of other species (1) are defined for the fuel densities ($\bar{\rho}_F^x = \bar{\rho} \tilde{Y}_F^x$) in the unburned (x=u) or burned (x=b) part. Transport equations for the mean (\bar{h}_s) and fresh gases (\tilde{h}_s^u) sensible enthalpies are also solved. Finally, in order to define correctly the species mass fractions in the unburned state for non-homogeneous mixtures, transport equations for the species tracers \tilde{Y}_{Ti} are introduced. Full details can be found in [18]. To avoid modifying the mixing processes involved in the species and energy transport equations outside the flame front a dynamic procedure allows to define the turbulent diffusivity at scale Δ_x out of the reaction zone. The mass filtered progress variable \tilde{c} can now be defined using the unburned and tracer fuel mass fraction (\tilde{Y}_{TF}):

$$\tilde{c} = 1 - \frac{\tilde{Y}_F^u}{\tilde{Y}_{TF}} \quad 3$$

The reaction rates appearing in the species, unburned fuel and sensible enthalpy transport equations are modeled following:

$$\bar{\rho} \tilde{\omega}_i = \rho_u \tilde{Y}_{Ti} S_L \bar{\Sigma} \quad 4$$

$$\bar{\rho} \tilde{\omega}_{h_s} = \sum_i \Delta h_i^0 \bar{\rho} \tilde{\omega}_i \quad 5$$

The laminar flame speed $S_L(\phi, T, p, \chi_{dil})$ is computed using a correlation proposed in 5.1 and 5.2. ρ_u is the mass density of unburned gases and Δh_i^0 is the enthalpy of formation of species i .

The transport equation for the flame surface density variable is:

$$\begin{aligned} & \frac{\partial \bar{\Sigma}_c}{\partial t} = \underbrace{-\nabla \cdot (\tilde{\mathbf{u}} \bar{\Sigma}_c)}_{T_{res}} - \underbrace{\nabla \cdot (S_D \bar{\mathbf{n}} \bar{\Sigma}_c)}_P + \\ & \underbrace{S_D \nabla \cdot (\bar{\mathbf{n}} \bar{\Sigma}_c)}_{C_{res}} + \underbrace{(\nabla \cdot \tilde{\mathbf{u}} - \bar{\mathbf{n}} \mathbf{n} : \nabla \tilde{\mathbf{u}}) \bar{\Sigma}_c}_{S_{res}} \\ & + \nabla \cdot \left(\left(\frac{v}{S_c} + \frac{\hat{v}_t}{S_{c_t}} \right) \nabla \bar{\Sigma}_c \right) \\ & + \underbrace{-\beta_0 S_L \frac{(\bar{\Sigma}_c - \bar{\Sigma}_{lam}) \bar{\Sigma}_c}{1 - \tilde{c}} + \beta_c S_L (1 + \tilde{\tau}) \frac{(\bar{\Sigma}_c - \bar{\Sigma}_{lam}) \bar{\Sigma}_c}{\tilde{c}}}_{C_{sgs}} \\ & + \underbrace{\alpha_{CFM} \Gamma \left(\frac{\hat{u}'}{S_L^0}, \frac{\widehat{\Delta}}{\delta_L} \right) \frac{\hat{u}'}{\widehat{\Delta}} \bar{\Sigma}_c}_{S_{sgs}} \end{aligned} \quad 6$$

$S_D = \rho_u \bar{\rho}^{-1} \bar{S}_L$ is the displacement speed. T_{res}, P, C_{res} and S_{res} are respectively the resolved transport term, the resolved propagation, resolved curvature and resolved strain term evaluated on the filtered flow field, and $\bar{\mathbf{n}} = -\nabla \tilde{c} / |\nabla \tilde{c}|$ is the normal to the iso-surface of the filtered progress variable. \bar{S}_L is the laminar flame speed, equal to S_L^0 in the absence of stretch model. The Reynolds and Favre filtered progress variables are related following:

$$\bar{c} = \frac{(1 + \tau) \tilde{c}}{1 + \tau \tilde{c}} \quad 7$$

with $\tau = \rho_u / \rho_b - 1$.

T_{sgs}, C_{sgs} and S_{sgs} are respectively the subgrid-scale diffusive transport term, the curvature term and the strain term which are modelled. $\bar{\Sigma}_c$ is a modified surface density [4,15,19]. $\bar{\Sigma}_{lam} = |\nabla \tilde{c}| + (\tilde{c} - \bar{c}) \nabla \cdot \bar{\mathbf{n}}$ is the laminar part of $\bar{\Sigma}_c$. The later S_{sgs} term involves a calibration parameter α_{CFM} and an efficiency function Γ modelling the influence of vortices on unresolved flame strain.

Note that these equations are filtered at a filter size $\widehat{\Delta} = n_{res} \Delta_x$ within the flame front. Moreover resolved eddies smaller than $\widehat{\Delta}$ are not able to wrinkle the flame front, but their effects on the flame are taken into account in the subgrid-scale strain through the efficiency function Γ .

Finally the subgrid-scale turbulence \hat{u}' involved in the function Γ is not evaluated based on the subgrid-scale eddy viscosity, whose aim is to dissipate the eddies smaller than Δ_x . Instead \hat{u}' is evaluated based on an operator acting on the resolved flow field $\hat{u}' = OP_2(\bar{\mathbf{u}}) = c_2 \Delta_x^3 \nabla^2 (\nabla \times \bar{\mathbf{u}})$ with $c_2=1.92$. More details can be found in [20].

We use the Γ efficiency function developed by Bougrine et al. [21].

2.2 Ignition model

The ignition process is modeled by the ISSIM-LES model (Imposed Stretch Spark Ignition Model) [22]. This model is based on the same electrical circuit description as AKTIM [23].

During the ignition phase, the flame kernel is typically smaller than the local grid size and is modelled by the ISSIM-LES model.

The flame kernel growth is modelled thanks to a modified flame surface density (FSD) equation and a transition factor α to ensure a transition from the SGS ignition kernel to the fully resolved turbulent flame. $\alpha(x, t)$ is 0 at ignition time and reaches 1 when ignition is over. The equation 6 is replaced by

$$\frac{\partial \bar{S}_c}{\partial t} = T_{res} + T_{sgs} + S_{sgs} + \alpha C_{sgs} + \alpha(C_{res} + S_{res}) - \nabla \cdot (\alpha S_D \bar{\mathbf{n}} \bar{S}_c) + (1 - \alpha) 2r_b^{-1} (1 + \tau) \Xi S_L \bar{S}_c + \bar{\omega}_\Sigma^{ign} \quad 8$$

where $2r_b^{-1}$ is the modelled curvature of the early flame kernel, τ the expansion factor and Ξ is a turbulent wrinkling factor defined in [22].

2.3 Stretch model

In lean or diluted conditions, the effect of the stretch on the laminar flame speed is not negligible, especially during the ignition phase where the flame is highly curved and stretched by the flow [24]. In this section, we propose to take into account this effect. In laminar flows, this model is usually based on a Markstein-type correlation using a linear relationship between the laminar flame speed and flame stretch [25]:

$$S_L = S_L^0 - \mathcal{L}_u K \quad 9$$

where S_L^0 is the un-stretched laminar flame speed, K is the total laminar stretch rate and \mathcal{L}_u is the Markstein length which depends on the composition, pressure and temperature of the mixture. In turbulent flows, if the validity of the Markstein length for turbulent flamelets is assumed and the probability density function of the stretch rate along the subgrid-scale turbulent flame front pdf(\tilde{K} , K_{sgs}) is known, \bar{S}_L can be written [26]:

$$\bar{S}_L = S_L^0 - \int_{K_{min}}^{K_{max}} \mathcal{L}_u \text{pdf}(K, \tilde{K}, K_{sgs}) dK \quad 10$$

However the knowledge of the pdf as a function of the mean and subgrid-scale stretch rate is unknown, as well as the limit values K_{min} and K_{max} of the Markstein lengths may also be affected by the non-uniformity of the stretch rate. Investigations on these effects is out of the scope of the present study. Moreover, the effect of the Markstein length on the laminar flame speed is attenuated with an increase of the turbulent intensity [26,27]. In spark-ignition engines, the effect of the Markstein length is likely to be higher during the early ignition when the flame front is highly stretched but weakly wrinkled by the subgrid scale turbulence. For this reason, the stretched laminar flame speed is estimated using the resolved contribution of the stretch rate. One possible approach is to assume that the laminar flame speed is locally in equilibrium with the local resolved stretch rate:

$$S_L^{eq} = S_L^0 - \mathcal{L}_u \tilde{K} \quad 11$$

In the present approach, $\tilde{K} = \alpha(C_{res} + S_{res})/\bar{S}_c + (1 - \alpha)2r_b^{-1}(1 + \tau)\Xi S_L$ with C_{res} and S_{res} representing respectively the resolved curvature and the resolved strain rate term in the flame density transport equation 6. The third right hand side term is the stretch induced by the modelled curvature given by ISSIM-LES. $\alpha(x, t)$ is the transition variable of the ISSIM-LES model. For sake of simplicity, we assume that the Markstein length relative to curvature and strain are the same: $\mathcal{L}_{u,c} = \mathcal{L}_{u,s} = \mathcal{L}$. Please note that the Markstein lengths evaluated in Section 3 are defined relative to the curvature.

As the filtered stretch rate depends on the laminar flame speed, an implicit formulation of equation 11 is solved following:

$$S_L^{eq} = \frac{S_L^0 - \mathcal{L}_u \alpha S_{res} / \bar{S}_c}{1 + \mathcal{L}_u \left(\alpha \frac{\rho_b}{\rho} \nabla \cdot \bar{\mathbf{n}} \right)} \quad 12$$

As stated earlier the equation 11 is assumed valid at equilibrium, when chemical time scale are similar or smaller in magnitude compared to transport time scale. Due to the intrinsic nature of turbulent flames, this hypothesis does not hold in turbulent combustion.

In order to take into account the transition to equilibrium a modelled transport equation is proposed for quantity $\tilde{\zeta} = \tilde{c} * \tilde{Y}_{TF} * \bar{S}_L$. An exact transport equation would be difficult to derive. Therefore, we propose a simple model equation following the work of Tabor and Weller [28,29] and Colin and Truffin [22] assuming that $\tilde{\zeta}$ is convected and diffused as a passive scalar and that its reaction rates can be deduced from the following decomposition $\frac{d\tilde{\rho}\tilde{\zeta}}{dt} =$

$$\tilde{Y}_{TF} \bar{S}_L \frac{d\tilde{\rho}\tilde{c}}{dt} + \tilde{\rho}\tilde{c} \tilde{Y}_{TF} \frac{d\bar{S}_L}{dt}.$$

The first RHS is easily written as follows:

$$\tilde{Y}_{TF} \bar{S}_L \frac{d\tilde{\rho}\tilde{c}}{dt} = \bar{S}_L \bar{\omega} \quad 13$$

where $\bar{\omega} = \rho_u \bar{S}_L \bar{S}_c$ is the progress variable source term.

The second term is formulated as a relaxation term in equation 12 assuming that the characteristic time before reaching equilibrium cannot be smaller than the chemical time $\tau_f = \delta / S_L^0$, where δ is the diffusive flame thickness estimated as $\delta = \lambda_u / (\rho_u C_p u S_L^0)$ [30,31],

$$\tilde{\rho}\tilde{c} \tilde{Y}_{TF} \frac{d\bar{S}_L}{dt} \approx \tilde{\rho}\tilde{\zeta} \frac{1}{\bar{S}_L} \frac{S_L^{eq} - \bar{S}_L}{\tau_f} \quad 14$$

Finally the transport equation for ζ is written following:

$$\frac{\partial \tilde{\rho}\tilde{\zeta}}{\partial t} + \frac{\partial \tilde{\rho}\tilde{u}_i \tilde{\zeta}}{\partial x_i} = \frac{\partial}{\partial x_i} \left(\left(\frac{\mu}{Sc} + \frac{\hat{\mu}_t}{Sc_t} \right) \frac{\partial \tilde{\rho}\tilde{\zeta}}{\partial x_i} \right) + \tilde{\rho}\tilde{\zeta} \frac{S_L^0}{\delta} \left(\frac{S_L^{eq}}{\bar{S}_L} - 1 \right) + \bar{S}_L \bar{\omega} \quad 15$$

At each time step, the stretched laminar flame speed is computed from equations 12 and 15 after the computation of the divergence of the normal $\nabla \cdot \bar{\mathbf{n}}$ and of the resolved strain rate. Then the resolved curvature C_{res} and the propagation term in the FSD equation as well as the reaction source terms are updated afterwards. Regarding the subgrid-scale terms, the stretched laminar flame speed is used in the curvature term C_{sgs} , whereas the Γ efficiency function of the subgrid-scale strain term S_{sgs} is evaluated with the un-stretched laminar flame speed. The justification of this choice would rely on detailed studies implying DNS, which are out of the scope of the present work.

3 FLAMELET CALCULATION

3.1 Objectives

The first objective of this section is to tabulate the laminar flame speed and the flame thickness covering both the ultra-lean and stoichiometric conditions (section 3.2). To this purpose we consider the combustion of a premixed iso-octane / air mixture and the detailed chemical kinetic mechanism ‘‘iso-octane, Version 3’’ developed at Lawrence Livermore National Laboratory is used [32-34]. The second objective is to derive a correlation for the Markstein number (section 3.6) over a wide range of pressure, temperature and fuel-air equivalence ratio with a lighter model developed by Cai et al. [35,36]. Finally, the Markstein length table is reconstructed by multiplying the tabulated flame thickness table and the Markstein number correlation.

3.2 Un-stretched Flamelet Calculation

We consider here an un-stretched, planar, freely propagating flame in one dimension at steady state governed by equations in appendix [37]. The diffusion effect takes into account the multicomponent diffusion and the Soret effect. The calculations have been performed with CANTERA version 2.4 [38]. The detailed mechanism from [32-34] is used. The calculations are performed for pressure ranging from 1 bar to 150 bar, unburned gas temperature from 300 K to 1100 K and fuel-air equivalence ratio from 0.4 up to 2.5. The calculations have been validated against experimental results of spherical expanding flame presented in appendix 11.2.

3.3 Stretched Flamelet Calculation Setup

Stretching of a flame under curvature and strain can lead to differences in the behavior of the flame compared to an un-stretched, planar and purely one-dimensional flame. The stretch is generally defined as the fractional area change of a flame surface element, which moves with the flame propagation velocity:

$$K_A = \frac{1}{A} \frac{dA}{dt} \quad 16$$

Stretched flames are calculated following the methodology described in [39,40] for spherically expanding flames.

The flame propagation v_f of an iso-surface is the sum of the local laminar burning displacement S_l and flow velocity v

$$v_f = v + S_l \quad 17$$

Although expanding flames are essentially unsteady, assuming that the chemical time scale is much smaller than the transport time scale (thin reaction zone compared to preheat zone), it is possible to derive steady flamelet equations in a moving flame-adapted coordinate system. In this coordinate system, the flame is treated as a steady, freely propagating flame, which is solved as an eigenvalue problem similarly to an un-stretched flame.

Using the density ρ as the progress variable it can be shown [40] that the stretch rate is almost constant through the flame and equates:

$$K_A = \frac{2v_f}{r_f} \quad 18$$

Thus, the stretch is an input parameter of the flamelet set of equations.

The calculation of the Markstein lengths for a given set of unburned conditions P, T and λ consists in calculating flamelets of increasing stretch levels K , starting from 0. The flamelets are iteratively calculated initializing from the previous calculated flamelets' flow fields.

The Markstein lengths measure the gradient of the laminar flame speed relative to the stretch, either on the fresh gas side or on the burned gas side.

$$S_{l,u}(K) = S_{l,u}^0 - K \cdot \mathcal{L}_u + O(K^2) \quad 19$$

$$S_{l,b}(K) = S_{l,b}^0 - K \cdot \mathcal{L}_b + O(K^2)$$

On the fresh gas side of the un-stretched flame ($K = 0$ /s), we define a reference unburned temperature $T_u^0 = T(x_u^0)$ where $x_u^0 = x_i^0 - \delta^0$, δ^0 is the un-stretched flame thickness and x_i^0 is the point of maximal temperature gradient in the flame front.

For each value of the stretch K , the fresh gas laminar flame speed $S_{l,u}(K)$ is evaluated at the T_u^0 isotherm, while on the burned gas side $S_{l,b}(K)$ is evaluated at the 20 percent heat release point, 100 percent corresponding to the inner reactive zone. \mathcal{L}_u and \mathcal{L}_b are finally estimated by polynomial interpolation of $S_{l,u}(K)$ and $S_{l,b}(K)$.

The Markstein numbers are dimensionless numbers defined as the ratio between the Markstein length and the un-stretched flame thickness. $\mathcal{M}_u = \mathcal{L}_u / \delta^0$ and $\mathcal{M}_b = \mathcal{L}_b / \delta^0$.

3.4 Stretched Flamelet Calculation Validation

The calculations have been performed with CHEM1D. This program can perform 1D un-stretched and stretched flame simulations. It has been proven to give accurate results. More information about CHEM1D can be found in [41].

We consider here the surrogate kinetic mechanism developed by Cai et al. [35,36] which is originally based on the detailed mechanisms used in the previous section. This mechanism offers a tractable number of reactions for CHEM1D as well as the possibility to assess the effect of the fuel surrogate composition.

In practice, for each P, T and ϕ condition considered, a dozen of consecutive stretched flamelet calculations are performed. The evaluation of the Markstein length consists in the fitting of a second order polynomial in K , and retaining the linear coefficient.

Figure 1 illustrates stretched flamelets calculation results for an iso-octane/air mixture at $\lambda = 1/\phi = 1.83$, $P = 31$ bar, $T = 745$ K, in which we plot burned gas and fresh gas stretched laminar flame speed and the corresponding Markstein lengths. These conditions are representative of the in-cylinder mean conditions at spark timing in the lean condition configurations (case 2 and case 3). \mathcal{L}_u and \mathcal{L}_b are estimated from the evolution of $S_{l,u}(K)$ and $S_{l,b}(K)$ for stretch values varying from 0 /s to 900 /s.

In Figure 2 we compare the measured burned gas Markstein lengths [24] and calculated values at 2 bar and 473 K conditions from $\phi = 0.65$ to $\phi = 1.5$. The calculated values agree fairly well with experiment; although for $\phi < 0.65$ ($\lambda > 1.53$) no data is available.

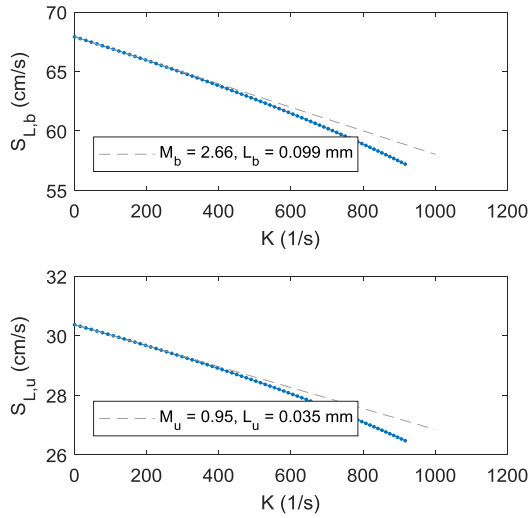


Figure 1
Burned gas laminar flame speed $S_{L,b}$ (above) and fresh gas laminar flame speed $S_{L,u}$ (below) for C_8H_{18} /air mixture as function of stretch, $\lambda = 1.83$, $P = 31$ bar, $T = 745$ K. For each case is plotted the regression line whose slope is the Markstein length: L_u in fresh gas and L_b in burned gas.

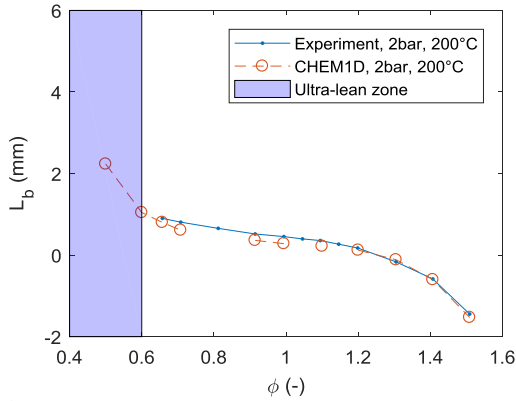


Figure 2
Burned gas Markstein length L_b as a function of ϕ for an iso-octane/air mixture at 2 bar and 473 K. Solid line: experiment, red dots: calculated Markstein lengths

3.5 Effect of surrogate composition on laminar flame speed and Markstein length at high dilution

The mechanism developed in [35,36] enables the definition of ternary surrogate mixtures composed of n-heptane, iso-octane and toluene; an optimal formulation based on the RON, MON and C/H ratio can be defined according to the analytical calculation method in [35]. Table 1 shows the composition of the considered surrogate in comparison to iso-octane. The RON, MON and H/C numbers were determined by characterization of the fuel blend used in the experiment.

Table 1
Properties and compositions of surrogate mixtures

Property	iso-octane	Surrogate
RON	100	100.1
MON	100	88.7
H/C ratio	2.25	1.78
n-Heptane [vol%]		9.3
iso-octane [vol%]	100	60.1
Toluene [vol%]		30.6

Figure 3 illustrates the effect of λ and the effect of the surrogate composition on the stretched laminar flame speed and Markstein length in ultra-lean conditions. The presence of toluene and n-heptane on the un-stretched laminar flame speed and Markstein length at $\lambda = 1.89$ (red and orange) is negligible and much smaller in comparison to the effect of increasing λ from 1.83 to 1.89 (blue and red). This result illustrates the fact that iso-octane is a suitable surrogate in lean condition.

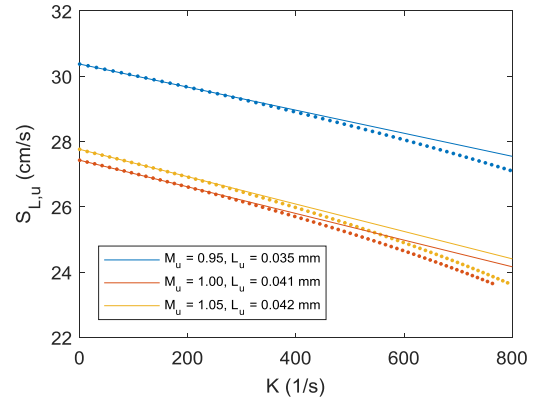


Figure 3
Stretched Laminar flame speed and Markstein length for fresh gas. Blue: iso-octane, $\lambda = 1.83$; red: iso-octane, $\lambda = 1.89$; orange: surrogate, $\lambda = 1.89$. $P = 31$ bar, $T = 745$ K in all 3 cases

3.6 Fresh gas Markstein Number Correlation

Here we focus on the effects of the stretch in the fresh gas side owing to the fact that the LES stretch model developed in next section requires laminar flame speed and Markstein length of the fresh gas only. The objective is to develop a correlation for the Markstein number in the form $\mathcal{M}_u = f(P, T_u, \phi)$.

3.6.1 Temperature effect

Figure 4 illustrates the fresh gas Markstein number at $P = 2$ bar for $T_u = 473$ K (conditions of Figure 2), $T_u = 800$ K and $T_u = 1100$ K. For each temperature we observe an inflection point situated at $\phi \cong 0.95$ and $Ma \cong 0.25$. For $\phi < 0.9$ the Markstein number decreases as the temperature increases while for $\phi > 1.0$ the opposite is visible. The evolution of the curve profiles suggests an asymptotical convergence to a line at high temperatures.

The curves $\mathcal{M}_u = f(\phi)$ are interpolated by a 3rd order polynomial in ϕ whose coefficients are $c_{T,i}$ $i = 0,1,2,3$. Figure 5 shows the evolution of each polynomial coefficient as a function of the temperature. A logarithmic fit in T_u is in turn applied to each of these coefficients.

Numerical values of the fitting parameters are presented in Table 2. Finally, the Markstein number is estimated by using equation 20.

$$\mathcal{M}_u = c_{T,3} \cdot \phi^3 + c_{T,2} \cdot \phi^2 + c_{T,1} \cdot \phi + c_{T,0} \quad 20$$

$$c_{T,i} = c_{T,i,0} + c_{T,i,1} \log(T_u/K)$$

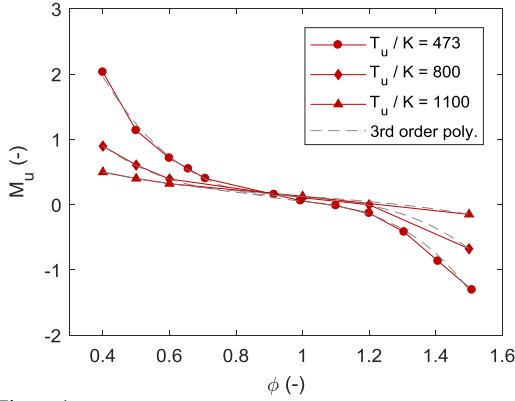


Figure 4
Fresh gas Markstein number \mathcal{M}_u as a function of ϕ at $P = 2$ bar: dots, $T_u = 473$ K; diamonds, $T_u = 800$ K; triangles, $T_u = 1100$ K; dashed line, best fit 3rd order polynomial

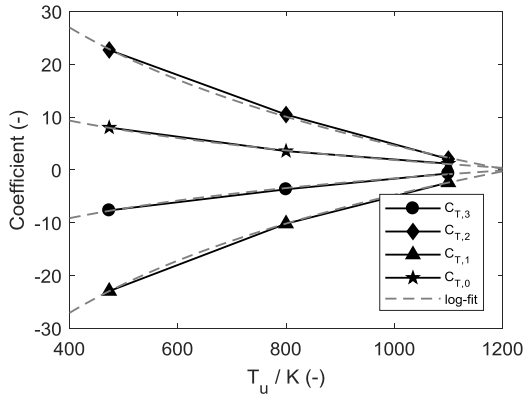


Figure 5
 $c_{T,i}$ coefficients as a function of T_u : star, $c_{T,0}$; triangle: $c_{T,1}$; diamonds: $c_{T,2}$; dot: $c_{T,3}$.

Table 2
Logarithmic fit coefficients for each coefficient of the third order polynomial for the temperature dependence

3 rd order polynomial coefficients $c_{T,i,j}$		
	$c_{T,i,0}$	$c_{T,i,1}$
constant term	58.06098121	-8.135279378
1st order term	-173.0600881	24.3670111
2nd order term	172.8656216	-24.35666842
3rd order term	-58.40616965	8.221030188

3.6.2 Pressure Effect

In the paragraph, we study the effect of pressure on the Markstein number at constant temperature $T_u = 800$ K relative to a reference pressure of 2 bar. Figure 6 illustrates the fresh gas Markstein number at 2, 10 and 20 bar. We can notice that \mathcal{M}_u increases with pressure. We consider $\mathcal{M}_{u,ref} = \mathcal{M}_{u, P=2 \text{ bar}, T=800 \text{ K}}$ as the reference Markstein from which we estimate the

variation as a function of the pressure. We apply a 3rd polynomial fitting in ϕ to $\mathcal{M}_u - \mathcal{M}_{u,ref}$. The dependence of each polynomial coefficient relative to the pressure is modelled by a 2nd order polynomial in $\log(P)$. Numerical values of the fitting parameters are presented in Table 3. $\mathcal{M}_u - \mathcal{M}_{u,ref}$ is estimated by using equation 21.

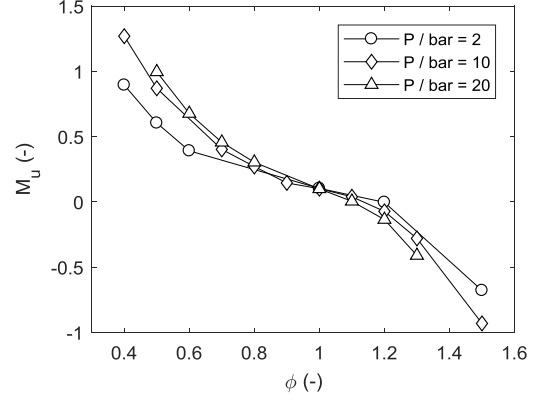


Figure 6
Fresh gas Markstein number \mathcal{M}_u as a function of ϕ at $T_u = 800$ K: dots, $P = 2$ bar; diamonds, $P = 10$ bar; triangles, $P = 20$ bar

Table 3
Coefficients of the logarithmic fit for each coefficient of the third order polynomial for the pressure dependence.

	3 rd order polynomial coefficients $c_{P,i,j}$		
	$c_{P,i,0}$	$c_{P,i,1}$	$c_{P,i,2}$
constant term	-0.18774	0.15038	0.173813
1 st order term	-0.02263	0.508155	-0.68602
2 nd order term	0.567828	-1.45509	0.917397
3 rd order term	-0.3479	0.779435	-0.40039

$$\mathcal{M}_u - \mathcal{M}_{u,ref} = c_{P,3} \cdot \phi^3 + c_{P,2} \cdot \phi^2 + c_{P,1} \cdot \phi + c_{P,0}$$

$$c_{P,i} = c_{P,i,0} + c_{P,i,1} \log\left(\frac{P}{1 \text{ bar}}\right) + c_{P,i,2} \log^2\left(\frac{P}{1 \text{ bar}}\right) \quad 21$$

3.6.3 Proposed correlation for \mathcal{M}_u

The proposed correlation consists in summing Equations 20 and 21:

$$\mathcal{M}_u = c_3 \cdot \phi^3 + c_2 \cdot \phi^2 + c_1 \cdot \phi + c_0 \quad 22$$

Where

$$c_i = c_{T,i,0} + c_{T,i,1} \log\left(\frac{T_u}{K}\right) + c_{P,i,0} + c_{P,i,1} \log\left(\frac{P}{1 \text{ bar}}\right) + c_{P,i,2} \log^2\left(\frac{P}{1 \text{ bar}}\right) \quad 23$$

3.6.4 Validation of the correlation

We observe a good agreement between the proposed correlation and the calculated Markstein number (Figure 7 and Figure 8). In Table 4 we compare the CHEMID results

and the correlation at pressure and temperature representative of the in-cylinder conditions at the ignition timing in lean conditions $\lambda = 1.83$ and $\lambda = 1.89$.

Table 4
Fresh gas Markstein number \mathcal{M}_u at ignition time conditions for $\lambda = 1.83$ and $\lambda = 1.89$

λ	P / bar	T / K	\mathcal{M}_u ChemID	\mathcal{M}_u Correlation
1.83	31	745	0.95	1.02
1.89	31	745	1.0	1.10

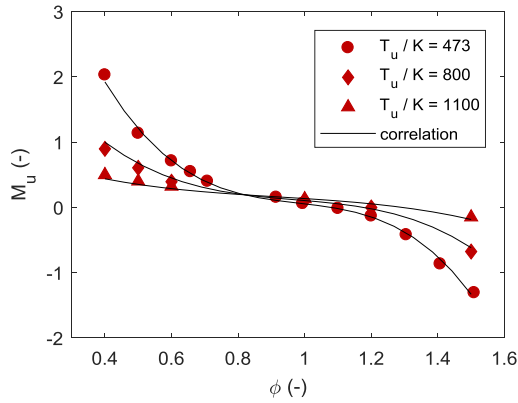


Figure 7
Comparison between CHEM1D calculated fresh gas Markstein number \mathcal{M}_u and the proposed correlation (continuous line) at $P = 2$ bar, $T_u/K \in \{473, 800, 1100\}$ and $0.4 \leq \phi \leq 1.5$: dots, $T_u = 473$ K; diamonds, $T_u = 800$ K; triangles, $T_u = 1100$ K.

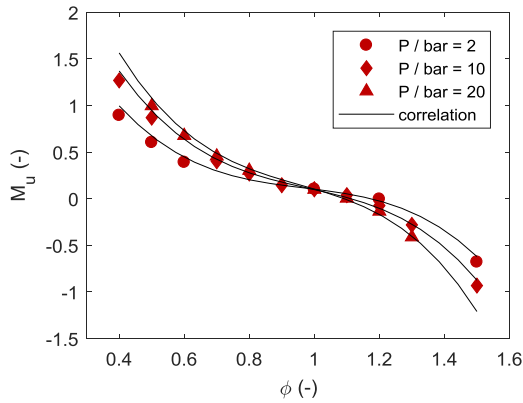


Figure 8
Comparison between CHEM1D calculated fresh gas Markstein number \mathcal{M}_u and the proposed correlation (continuous line) at $T_u = 800$ K, $P/\text{bar} \in \{2, 10, 20\}$ and $0.4 \leq \phi \leq 1.5$: dots, $P = 2$ bar; diamonds, $P = 10$ bar; triangles, $P = 20$ bar

3.7 Markstein length reconstruction and EGR effect

The fresh gas Markstein length is reconstructed by $\mathcal{L}_u = \mathcal{M}_u \cdot \delta^0$ where δ^0 is the un-stretched laminar flame thickness calculated with the detailed iso-octane mechanism. \mathcal{M}_u is calculated with the proposed correlation. The effect of residual gas dilution on the laminar flame speed is classically modelled by a linear correction $S_L^0 = S_L^{X_{dil}=0} (1 - 2.43X_{dil})$ where X_{dil} is the

residual gas molar fraction. By assuming the flame thickness is inversely affected, the Markstein length becomes $\mathcal{L}_u = \mathcal{L}_u^{X_{dil}=0} / (1 - 2.43X_{dil})$. The linear coefficient has been determined by averaging the first order interpolation coefficient over the ranges: $0.4 < \phi < 1.2$, $300 \text{ K} < T < 1100 \text{ K}$, $1 \text{ bar} < P < 101 \text{ bar}$, $X_{dil} < 0.1$.

4 TEST ENGINE SPECIFICATIONS

The base configuration is a central injection single-cylinder research engine, which has been jointly developed by TGR-E (TOYOTA GAZOO Racing Europe GmbH) and FEV [42,43]. The engine specifications are listed in Table 5.

There are two hardware configurations which differ mainly by piston shapes: a stoichiometric version and a lean configuration operating at $\lambda = 1.83$. Three cases are considered (Table 6): Case 1 is the stoichiometric configuration, which is used as a reference case for which the spark-plug electrodes lie in the reference tumble plane. This case features well-known conditions where LES models have been previously tested and validated. Cases 2 and 3 are computations of the lean configuration with two possible orientations of the spark plug. Case 2 (resp. case 3) features a transverse situation (resp. parallel situation) of the electrodes with reference to the tumble plane. Figure 9 presents a cross-sectional view of the engine showing the cylinder head and the combustion chamber in the stoichiometric configuration. A triple pressure analysis of the mean cycle (phase average cycle) is performed to calibrate intake pressure, effective compression ratio and in-cylinder pressure shift. A multi-cycle pressure analysis is then performed on both $\lambda = 1.83$ and stoichiometric cases to extract the individual cycles' burning rate. We underline here that the exact spark plug orientation during the experiment in lean burn is not known, while it was for the stoichiometric version. This motivates the study on the effect of the spark plug orientation on the combustion process.

Table 5
Engine Specifications

Bore / Stroke	85.5 / 101.5 mm
Displacement	583 cm ³
Geometrical CR	13.4
Valves & Intake Ports	4 with intake VCM
Intake Camshaft	3 different lifts & durations
Ignition System Energy	max. 500 mJ
DI Injector	7 holes
Injection Pressure	max. 500 bar
Fuel's Octane Quality	100 RON

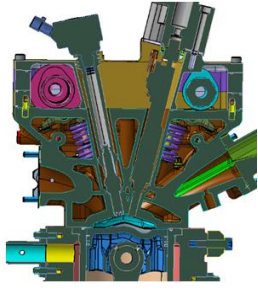


Figure 9
Cross section of engine's head-combustion chamber in the tumble
plane

Table 6
Computational domain and operating conditions

Case	λ	Tumble plane cross section of the combustion chamber	Overview of geometry	Spark-plug orientation	Boost pressure / bar	RPM	Spark timing / CAD	Ignition Energy / mJ	Number of experimental cycles
1	1.00			parallel	1	1500	-6.8	150	480
2	1.83			⊥ transversal	1.668	1900	-20.3	500	1000
3	1.83			parallel					

5 LES NUMERICAL SETUP

5.1 Computational domain

The computational domain comprises the combustion chamber, the intake and exhaust ports. As described in [43] intake and exhaust boundary conditions are imposed on planes situated at the positions of the low-pressure measurement sensors of the experiment.

5.2 Numerical Setup

The calculations are performed using the AVBP LES compressible solver, which solves explicitly the Navier-Stokes equations on unstructured grids. The finite volume Lax-Wendroff convective scheme (LW) (second order in time and space) with an explicit time advancement is used [44].

AVBP handles piston engine simulations of moving meshes with tetrahedral cells (ALE) [45] with the use of the automatic body fitted hybrid mesh generator OMEGA [46]. Crank-angle resolved pressure, constant temperature and species mass fractions are imposed at inlet and outlet using the NSCBC formalism (Poinsot & Lele) for the inlet/outlet boundary conditions [47]. The walls are treated as isothermal with a no-slip wall formulation [48,49]. Finally, the subgrid-scale turbulence is modelled using the Sigma model [17].

5.3 Mesh setup

Table 8 illustrates the mesh length scales in the ports and combustion chamber at each stroke. During the injection phase a specific additional refinement around the injector cone is activated [43].

The same methodology is applied to all the three configurations considered in this study.

5.4 Ignition set-up

The engine is equipped with an electronic high-energy ignition system together with a conventional spark plug [43]. The discharge energy and dwell time can be adjusted. The ISSIM-LES model [22] used for the modeling of the ignition process includes an inductive secondary electrical circuit whose secondary resistance has been adjusted for both lean and stoichiometric cases to reproduce a five CAD long arc in the lean cases and one CAD in the stoichiometric case (Table 7).

Table 7
Secondary circuit modelling

Case	Energy / mJ	Estimated arc duration / ms	Secondary resistance / Ω	Secondary inductance / H
Stoichiometric	150	0.12	150e4	30
Lean	500	0.44	25e4	30

5.5 Injection set-up

The injected spray is modelled using a Lagrangian formalism [50] to represent the liquid phase. The droplet size distribution resulting from primary atomization is approximated by a Rosin-Rammler distribution, imposed at the injector outlet. A two-way coupling between the gaseous and the dispersed phase is taken into account. The secondary break-up is modelled using the SAB model [51]. Fuel evaporation is modelled following Abramzon Sirignano [52]. The same calibrated model is used in the three considered cases. More details on injector spray pattern and model calibration details can be found in [43].

Table 8

Mesh length scale definition. The inlay indicates the refinement conditions in the spark plug area during the combustion. The distance r is relative to the mid-point between electrodes. The refinement are activated several CAD before spark timing.

Engine Stroke	Intake /mm	Compression /mm	Combustion /mm	Expansion /mm
Intake Port	0.3~0.5	0.5~0.7	0.7	0.8
Combustion chamber	0.65	0.65	<div style="border: 1px solid black; padding: 2px; display: inline-block;"> 0.1 $r _{sp} < 3\text{mm}$ 0.25 $r _{sp} < 6\text{mm}$ 0.4 $r _{sp} < 10\text{mm}$ 0.5 </div>	0.75
Exhaust port	0.5~2	0.5~2	0.5~2	0.5~2

5.6 Methodology

Table 9 summarizes the LES methodology for each case. Case 2 relies on consecutive cycles previously calculated in [43] for lean burn combustion. For each cycle “n”, the combustion phase is simulated starting from the solution of cycle “n” a few CAD before ignition and using laminar flame speed and Markstein length correlations presented in this paper.

Case 3 differs from case 2 by the orientation of the spark plug. In order to save calculation time, we start each cycle at scavenging TDC, initializing by mapping the flow fields from each cycle of case 2 (Figure 10). Figure 11 illustrates the mapping of the temperature field. Momentum, pressure and species’ mass fraction are likewise mapped.

For each case, the number of considered cycles does not include initialization cycles for convergence of the trapped mass and residual gas.

Table 9

LES methodology for considered cases.

Case	λ	Spark plug	Methodology	number of considered cycles
1	1		Consecutive cycles	10
2	1.83	⊥	Combustion phase of existing consecutive cycles	12
3	1.83		Mapping from case 2 at scavenging TDC	10

α_{CFM} is a model parameter which must be calibrated. Table 10 shows the values used in all the three cases. The independence of consecutive cycles is a prerequisite to the validity of the mapping strategy presented above to calculate case 3’s cycles from cycles of case 2. The correlation coefficient between 900 consecutive cycles’ CA50 is 0.004 (Figure 29); for the burn duration CA10-75, the coefficient is 0.1 (Figure 30). Therefore, the methodology presented above is valid in this case.

Table 10

α_{CFM}

Case	λ	Spark plug orientation	α_{CFM}
1	1		0.6
2	1.83	⊥	0.4
3	1.83		0.4

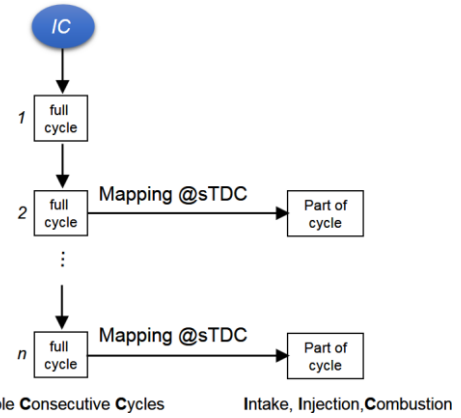


Figure 10

Calculation methodology for case 3.

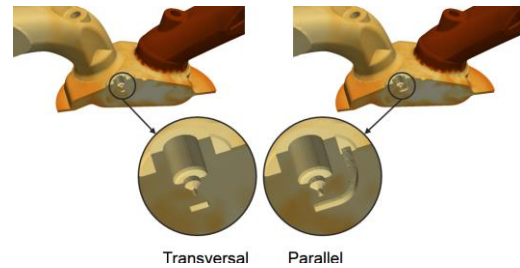


Figure 11

Mapping of temperature field from the ⊥ transversal to the || parallel configuration

5.7 LES Resolution

Different quantitative criteria have been proposed in literature in order to assess a posteriori the quality of a LES [53,54]. However, a practical difficulty is the absence of an estimation of the dissipation, which is necessarily introduced when numerically solving the filtered model

equations. This can be illustrated by introducing the effective Reynolds number of the simulated flow

$$Re_{eff} = \frac{\rho UL}{\mu_{eff} = \mu_{mol} + \mu_{Turb} + \mu_{num}} \quad 24$$

μ_{eff} is the effective viscosity of the simulated flow, μ_{mol} the molecular viscosity, μ_{Turb} the turbulent viscosity estimated from the subgrid-scale model and μ_{num} the numerical viscosity depending on the numerical approach used in the resolution process.

A very high quality LES would be achieved when the level of μ_{eff} is of the order of μ_{mol} , implying a μ_{Turb} of the order of μ_{mol} and a negligible μ_{num} .

In practice, any attempt to apply such a criterion fails owing to the impossibility to yield a reliable local instantaneous estimation of the dissipation introduced by the numerical approach.

We nevertheless propose a qualitative illustration of the achieved LES resolution in our simulations by plotting instantaneous fields of the ratio μ_{turb}/μ_{mol} . Assuming a sufficiently low level of numerical dissipation achieved by the present explicit second order numerical approach, this allows highlighting the regions where the LES resolution

is comparatively high or low. It should be noted that the level of resolution of combustion phenomena could not be thus achieved.

Figure 12 shows instantaneous field of μ_{turb}/μ_{mol} in a vertical cut-plane through the intake valve for a selected cycle of cases 1 and 3

In the lean case 3, the maximum ratio of around 50 in the intake stroke is reached in the intake jet and close to walls, with much lower values (and this relatively higher resolution) in the rest of the chamber. During the compression stroke, higher values are achieved, in the last 30 CAD before TDC, indicating a lower LES resolution of the smaller eddies created by the tumble breakdown.

In the stoichiometric case 1, the maximum values are globally smaller than those found in case 3, as a direct consequence from the lower load and RPM that result in comparatively larger smallest eddies, leading to a higher LES resolution on the same mesh.

Even if this can indeed not be used to draw any quantitative conclusions on the achieved LES quality, we nevertheless concluded that our LES approach appears to yield an acceptable resolution of key phenomena as the intake jet and the tumble breakdown.

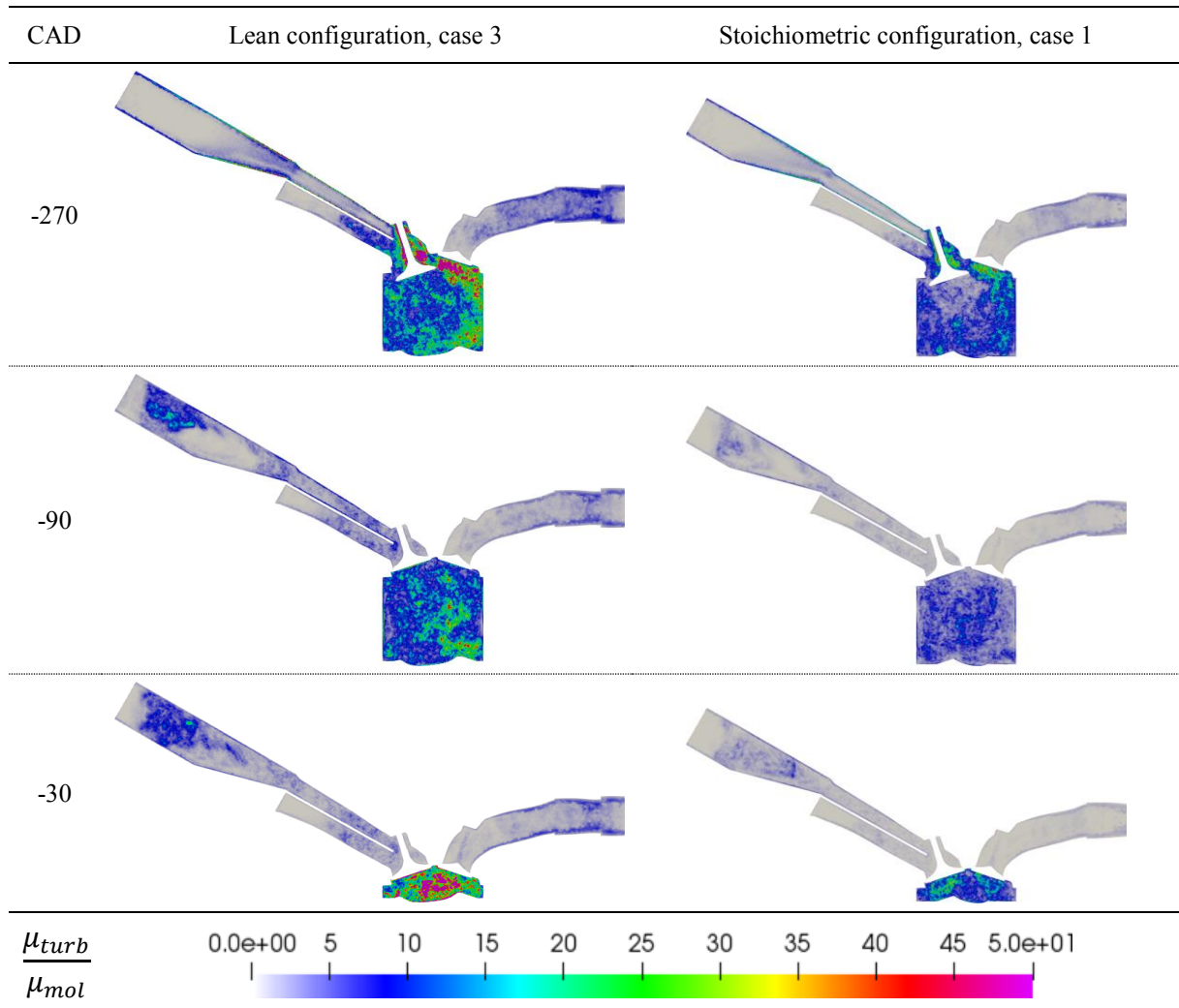


Figure 12

Mesh resolution expressed in terms of turbulence viscosity to molecular viscosity ratio for both the lean case 3 and stoichiometric case 1 in a plane parallel to the tumble plane and passing through the intake valve axis.

6 LES RESULTS AND ANALYSIS

6.1 Analyses of the cycle-to-cycle variations

The objective is here to compare experimental and simulated results in terms of key quantitative metrics of the combustion process. Regarding the early flame development, of particular interest in lean burn combustion, we consider the 2 percent burning point (CA2). For the burn duration, we consider the interval between the 10 percent burning point and the 75 percent burning point (CA10-75) rather than the commonly adopted CA10-90 to mitigate the effect of the heat transfer occurring in the second part for the combustion. Lastly, we take into account the 50 percent burning point (CA50).

6.1.1 Qualitative comparison to experiment

In Figure 13, we compare the calculated in-cylinder pressure of case 2 (\perp transversal lean burn) to the experimental pressure traces. One can observe that all pressure curves lie within the envelope. During the expansion phase, the pressure curves are higher. We attribute this to the blow-by [43] of the research engine, not modelled in the LES simulation. In Figure 14, we compare the mean pressure curves and its deviations (mean pressure \pm standard deviation). As a main result, the mean pressure curve is very close to the experimental pressure. The pressure deviation obtained by the LES simulation is very close to the experimental one although only 12 cycles are considered.

Figure 15 and Figure 16 illustrate respectively the distribution of CA50 versus CA2 and CA10-75 versus CA50 for the three cases against experimental data. In the stoichiometric configuration, a fair correlation is obtained. In the lean configuration, the numerical results of case 2 (\perp transversal) yield a variation range similar to that of the experimental clouds of points, while it is about twice smaller in case 3 (\parallel parallel). In both cases, the orientation of the cloud of points is similar to the experiment. This is illustrated by the regression lines of case 1 and case 2.

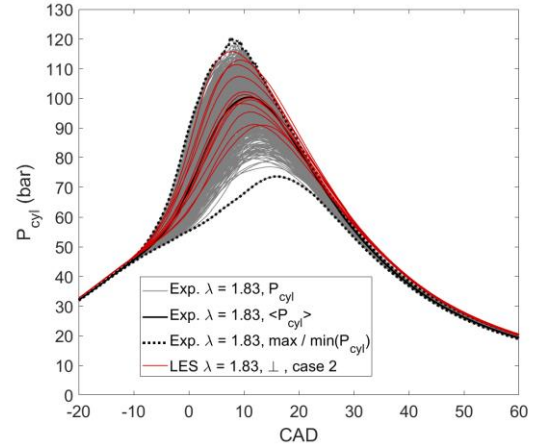


Figure 13

In-cylinder pressure comparison. Gray curves, experimental data $\lambda = 1.83$; black line, mean experimental pressure; dotted lines, experimental pressure envelope; red lines, in-cylinder pressure LES case 2 (lean, \perp configuration)

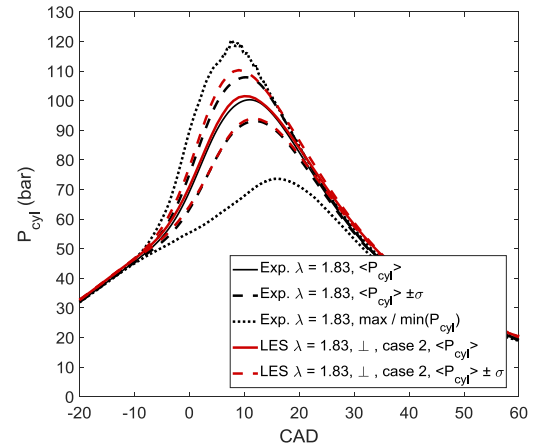


Figure 14

In-cylinder pressure comparison. Black curves; experimental pressure $\lambda = 1.83$; red curves: in-cylinder pressure LES case 2 (lean, \perp configuration). Continuous lines, mean pressure; dashed lines, mean pressure \pm standard deviation; dotted lines, experimental pressure envelope.

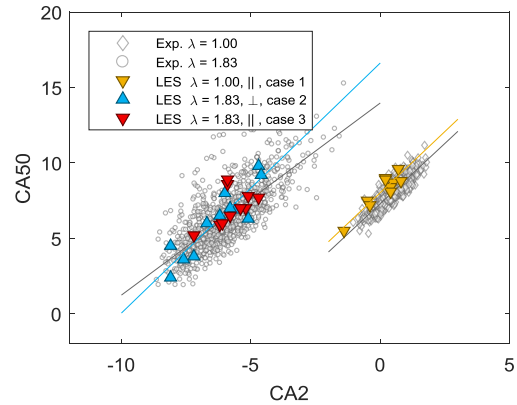


Figure 15

CA50 vs CA2, Gray diamonds: experimental data $\lambda = 1.0$; Gray dots: experimental data $\lambda = 1.83$; orange triangles, LES case 1 (stoichiometric, \parallel configuration); blue triangles, LES case 2 (lean, \perp configuration); red triangles, LES case 3 (lean, \parallel configuration);

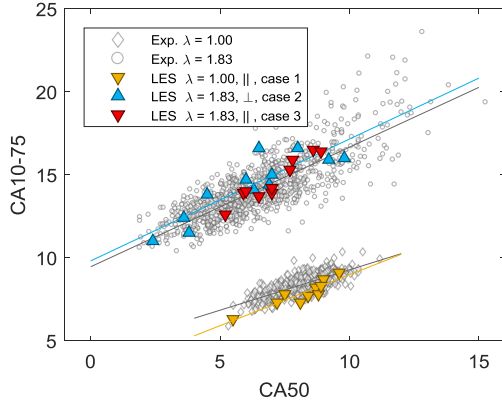


Figure 16
CA10-75 vs CA50, Gray diamonds: experimental data $\lambda = 1.0$; Gray dots: experimental data $\lambda = 1.83$; orange triangles: LES case 1 (stoichiometric, \parallel configuration); blue triangles: LES case 2 (lean, \perp configuration); red triangles: LES case 3 (lean, \parallel configuration).

6.1.2 Statistical comparison to experiment

In what follows, we compare the mean and the standard deviation of CA0-2, measuring the interval between the spark timing and the 2 percent burning point, CA50 and CA10-75.

1. Case 1 (Stoichiometric, \parallel parallel): Fair agreement between simulation and experimental data (Table 11).
2. Case 2 (Lean, \perp transversal): We observe a good correlation between experiment and calculation, in terms of both mean and variability (Table 12).
3. Case 3 (Lean, \parallel parallel): Compared to the experiment, the mean CA50 is ~ 1 CAD later and the mean CA10-75 is ~ 0.8 CAD longer (Table 13). More remarkably, the variability of the combustion process is approximately fifty percent lower compared to the experiment and case 2. We speculate that this particular spark plug orientation protects the early flame kernel development from side flow and turbulence. This analysis will be developed in section 6.3.1.

We notice that CA0-2 is two times larger in the lean cases (both experiment and LES) than in the stoichiometric case. A longer CA0-2 in lean conditions is indeed expected due to a smaller laminar flame speed and a positive Markstein number.

Table 11
Case 1 (\parallel parallel stoichiometric), Mean and standard deviation of CA0-2, CA50 and CA10-75

	CA0-2	CA50	CA10-75
Mean LES \parallel	6.9	8.2	7.8
Mean Experiment	7.3	8.1	8.3
σ LES \parallel	0.67	1.18	0.79
σ Experiment	0.53	0.97	0.63

Table 12
Case 2 (\perp transversal lean burn), Mean and standard deviation of CA0-2, CA50 and CA10-75

	CA0-2	CA50	CA10-75
Mean LES \perp	14.0	6.2	14.3
Mean Experiment	14.4	6.4	14.1
σ LES \perp	1.24	2.26	1.89
σ Experiment	1.21	2.06	1.83

Table 13
Case 3 (\parallel lean burn), Mean and standard deviation of CA0-2, CA50 and CA10-75

	CA0-2	CA50	CA10-75
Mean LES \parallel	14.6	7.1	14.6
Mean Experiment	14.4	6.4	14.1
σ LES \parallel	0.7	1.20	1.30
σ Experiment	1.21	2.06	1.83

6.2 Analysis of the initial flame kernel development and the influence of the stretch effect

We have seen in Section 3.4 that the dependence of the Markstein length towards the fuel-air equivalence ratio is highly nonlinear. In particular, the Markstein number varies following a third order polynomial towards lean condition (Section 3.6), while at the same time the flame thickness increases.

We illustrate the Markstein effect on case 2 (\perp transversal lean burn) by setting the Markstein length to null over the complete range of P, T_u, ϕ, Y_{res} conditions and recalculating the combustion phase. Figure 17 illustrates the effect of the null Markstein length on the in-cylinder pressure for the median cycle (red continuous line). The maximum pressure in that case increases by 9 bar. The pressure curves lies outside the mean \pm standard deviation zone and gets close to the maximum experimental pressure limit between -10 CAD and -5 CAD. In terms of heat release rate, one can observe in Figure 18 a shorter ignition delay by roughly 3 CAD. These results are in line with previously calculated results presented in [43].

A very convenient way to measure the effect of the stretch on the flame propagation is to compare the flame conditioned un-stretched laminar flame speed $S_{L,\Sigma}^0 = \int \Sigma S_L^0 / \int \Sigma$ and the flame conditioned effective laminar flame speed $S_{L,\Sigma} = \int \Sigma S_L / \int \Sigma$ where Σ is the flame surface density, S_L^0 the local un-stretched laminar flame speed, and S_L the effective laminar flame speed calculated by equation 15. Figure 19 shows $S_{L,\Sigma}^0$ and $S_{L,\Sigma}$ for both case 1 (stoichiometric) and case 2 (lean case) and Figure 20 shows the ratio $S_{L,\Sigma} / S_{L,\Sigma}^0$ measuring the global effect of the stretch on the flame speed. In both cases, the median cycle in terms of CA50 is considered.

In lean condition, the effect of the stretch is significant during the 20 CAD following the ignition, corresponding to the growth of the initial kernel subject to high stretch and flame curvature. The effect is maximal at -9 CAD for which the flame speed is reduced by 71% compared to the un-stretched laminar flame speed. In stoichiometric condition (case 1), the effect of the stretch is less than 5% and limited to the 5 CAD following the ignition.

To illustrate visually the stretch effect, we consider the local ratio of stretched to un-stretched laminar flame speed S_L / S_L^0 on the flame represented by an iso-surface of the progress variable $\tilde{c} = 0.2$. In lean condition (Figure 21, left

column), the effect of the stretch is visible in the early flame development at -19 CAD (1.3 CAD after spark timing). From -10 CAD to -5 CAD, the effect on the flame wrinkling is clearly visible owing to the fact that both resolved curvature and strain are considered in the stretch. In particular, at -5 CAD the ratio S_L/S_L^0 covers almost entirely the range from 0 to 1. In regions of negative curvature, the flame speed can be locally larger than the un-stretched laminar flame speed as can be seen at 0, 5 and 10 CAD in areas where the resolved stretch \tilde{K} is locally negative (Figure 21, right column). The resolved stretch includes the ignition term.

As expected from theory, the resolved stretch is mostly positive. Nevertheless, it can reach very locally negative values, owing to the calculation of the curvature based on the divergence of the normal to the surface, leading to numerical noise. The S_L/S_L^0 post-processing for the stoichiometric case is available in Appendix (Figure 24).

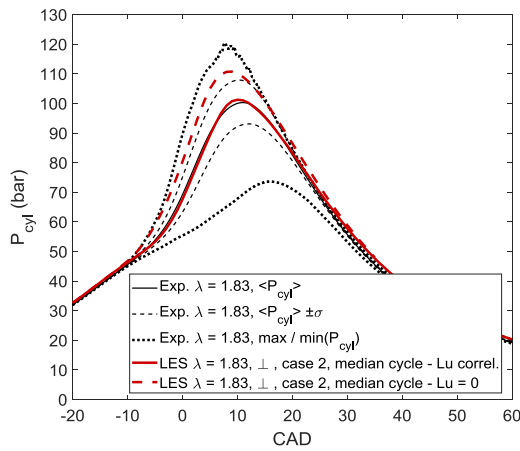


Figure 17
Effect of stretch on the in-cylinder pressure. Red line, CA50 median cycle (lean burn case 2); red dashed line, same cycle whose combustion phase has been calculated setting Lu to 0mm.

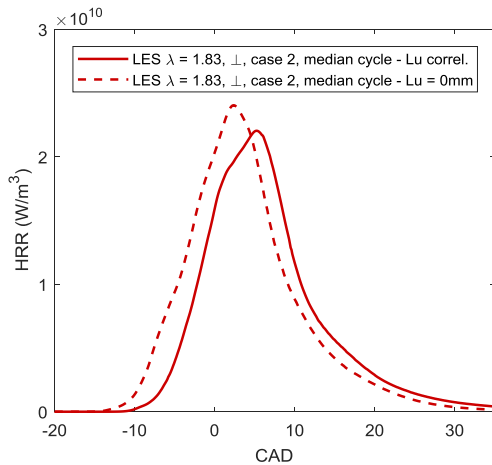


Figure 18
Effect of the stretch on the heat release rate per unit of volume. Continuous line, CA50 median cycle (lean burn case 2); dashed line, same cycle whose combustion phase has been calculated setting Lu to 0mm.

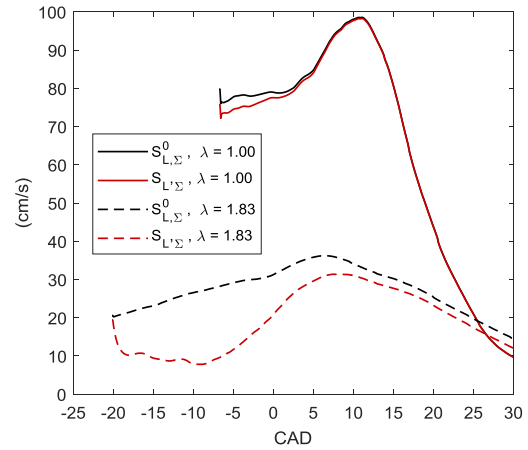


Figure 19
Evolution of the un-stretched laminar flame speed S_L^0 (black) and the effective laminar flame speed S_L (red) on the flame front. Solid line: Stoichiometric case 1; dashed line: lean burn case 2. For both cases, the median cycle in terms of CA50 is considered.

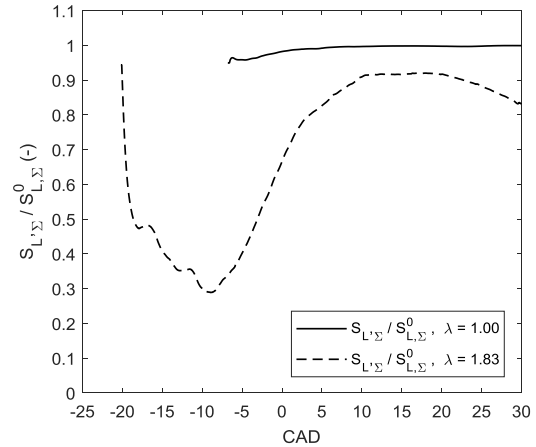


Figure 20
Evolution of $S_{L,\Sigma}/S_{L,\Sigma}^0$. Solid line: Stoichiometric case; dashed line: lean burn case 2 (same cycles as in Figure 19).

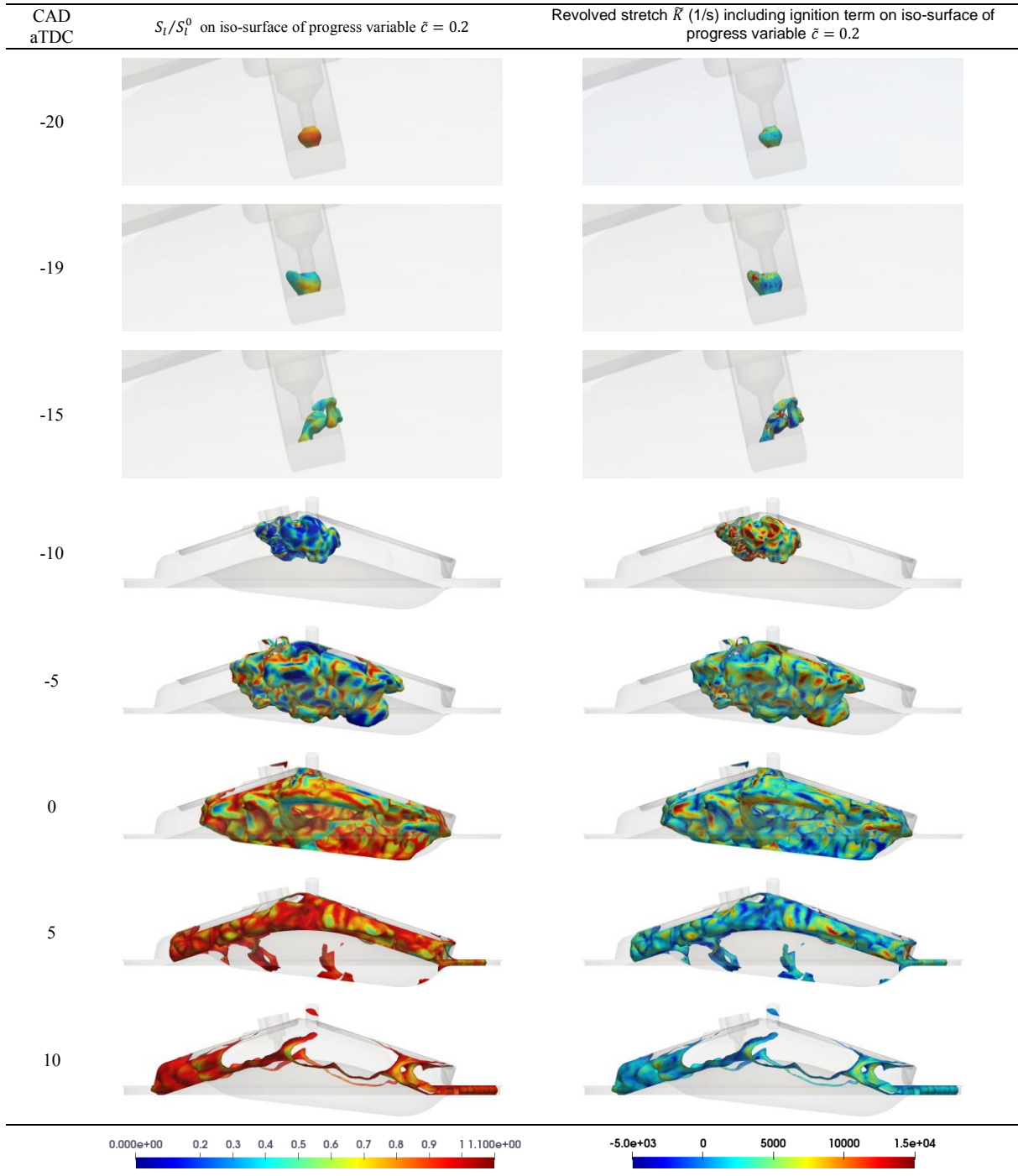


Figure 21

Evolution of flame propagation represented by Iso-surface of progress variable to $\tilde{c} = 0.2$ on median cycle of case 2 (according to CA50). Left column: iso-surface colored by S_t/S_t^0 . Dark red indicates no Stretch effect. Blue indicates stretch effect larger than 50 percent. Right column: revolved stretch including ignition contribution.

6.3 Study of extreme cycles in lean burn

6.3.1 Mean flow and turbulence

We perform a pointwise statistical analysis of the velocity field of all considered cycles at 20 CAD BTDC in the tumble plane. The mean flow velocity is normalized by the mean piston speed. The fluctuating velocity is calculated as the normalized RMS of the velocity fluctuation. The subgrid-scale turbulence is the normalized RMS of the subgrid-scale turbulence $\hat{u}' = OP_2(\bar{u})$ calculated

according the equation presented in Section 2.1 on each individual cycle.

We notice four main differences (Figure 22):

1. In case 2 (\perp configuration), the flow between the electrodes is pronounced ($u/c_m \sim 1.5$) and points towards the exhaust side. Instead, in case 3 (\parallel configuration), the flow is more quiet in the spark plug area, presumably due to the obstruction of the ground electrode.
2. The upper stream of the remaining tumble, directed to the exhaust side, is stronger in case 3 (\parallel

- configuration) with a clear recirculation zone to the right of the electrode (intake side).
3. The flow variability is significantly more intense in case 2 (\perp configuration).
 4. The subgrid-scale turbulence levels are similar in both cases, yet the center of gravity lies qualitatively 5mm more to the exhaust side in case 2.

It is likely that the higher flow variability in case 2 (\perp configuration) explains partly the larger spread of the combustion process. We can possibly infer that (1) is responsible for transfer of turbulence to the exhaust side (4) in the same configuration. Concerning the slower mean combustion process in case 3 (\parallel configuration), the weak recirculation zone to the right of the electrode (2) is likely to entrain the flow, and thus the flame, to the upper intake side where it could be blocked.

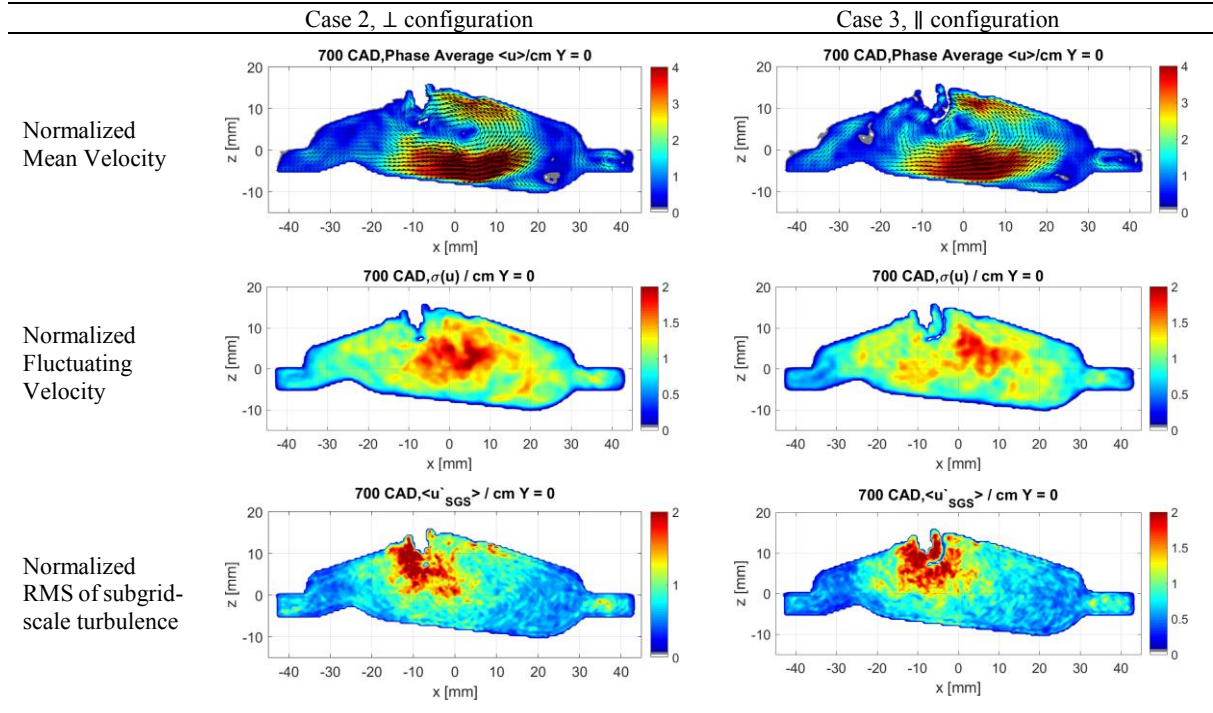


Figure 22
Mean, fluctuating flow and subgrid-scale turbulence at 20 CAD BTDC in the tumble plane and normalized by the mean piston speed. The Intake port is situated in the $x > 0$ domain. Left column: \perp configuration, case 2; right column: \parallel configuration, case 3. First row: Dimensionless mean flow (u/c_m), second row: dimensionless flow-variability (u'_{var}/c_m), third row: dimensionless RMS of subgrid-scale turbulence (u'/c_m). Note that the flow variability and subgrid-scale turbulence account for all the three velocity components.

6.3.2 Conditional Mean flow and turbulence

Here we consider the \perp configuration (case 2) which appears to be largely affected by the cycle-to-cycle variations. We select the three earliest and the three latest burning cycles in terms of CA2. The objective is to compare both sets in terms of conditional mean flow and conditional RMS of the subgrid-scale turbulence. In Figure 23, we observe two different flow patterns. For the late burning cycle the remaining tumble core is well formed with two strong streams, a lower stream pointing towards the intake side and an upper stream pointing towards the exhaust side. In the early burning cycle the upper stream is much weaker and the lower stream stronger. The effect of the upper stream on convection is visible in the turbulent distribution, shifted to the exhaust side for the later burning cycle. We hypothesize that the early flame undergoes two phenomena: The flame at early stages burns predominantly on the exhaust side, while being convected by the lower stream.

To illustrate this hypothesis, we analyze the flame propagation of two cycles, each representative of the late and early burning cycles' set. The cycles are chosen to have similar Fuel-Air equivalence ratio in the spark plug area at spark timing. In Figure 24, we actually observe that for Cycle 11 pertaining to the late burning cycle set, the flame develops slowly and exclusively on the exhaust side of the spark plug up to 5 CAD bTDC. On the other hand, for Cycle 15 the flame propagates spherically up to 5 CAD bTDC.

The similarity between the flow patterns of the late burning cycles in case 2 and the mean cycle of case 3 is possibly one of the reasons to the slower mean combustion process of case 3, even though the aerodynamic mechanism is different. In case 3, it is due to the electrode orientation, while in case 2 the exact mechanism is not clear.

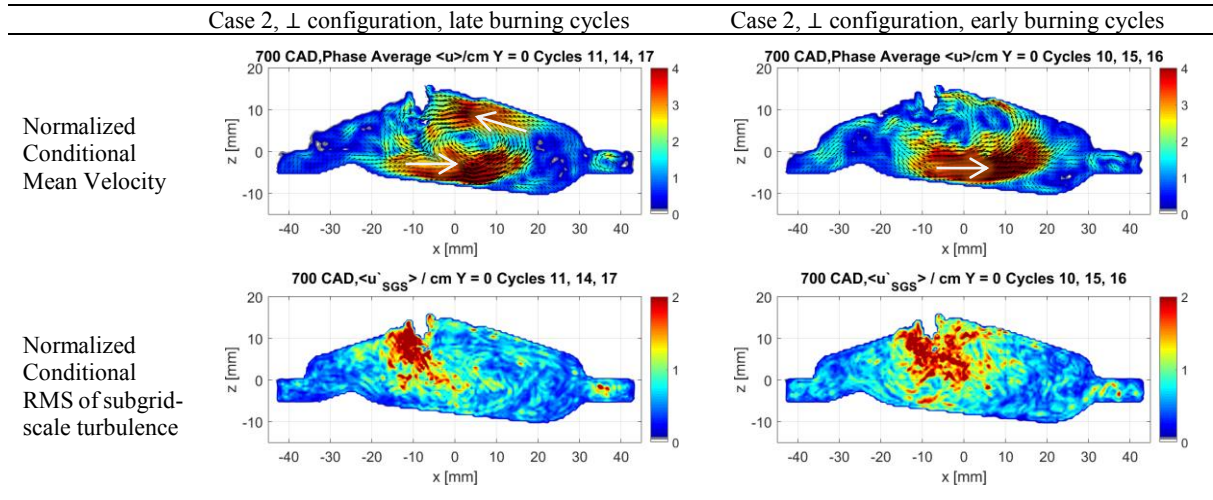


Figure 23

Mean and subgrid-scale turbulence at 20 CAD BTDC in the tumble plane, normalized by the mean piston speed. Left column: \perp configuration, case 2, late burning cycles; right column: \perp configuration, case 2, early burning cycles. First row: Dimensionless mean flow (u/c_m), second row: dimensionless RMS of subgrid-scale turbulence (u'/c_m).

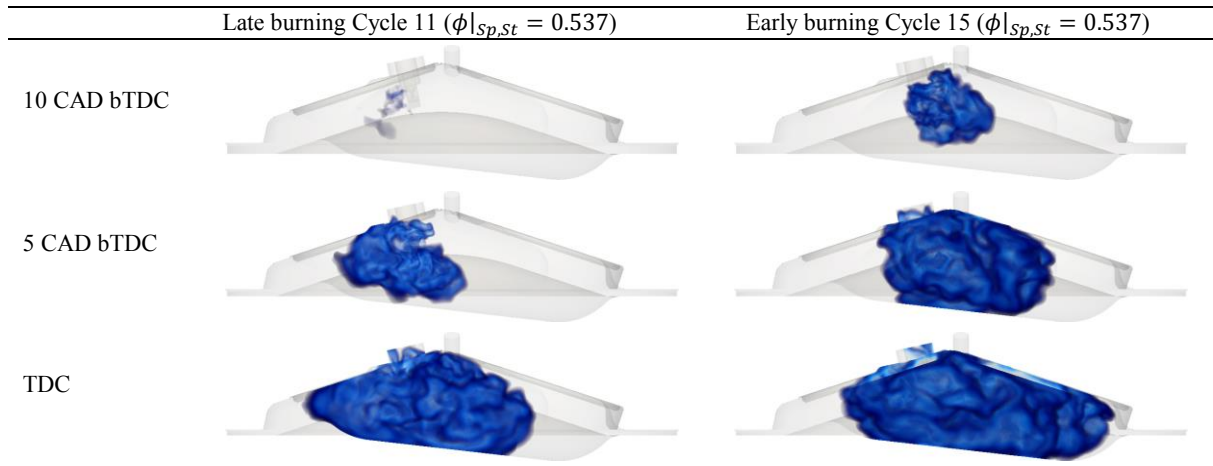


Figure 24

Volume rendering of the combustion progress variable (dark blue corresponds to $\tilde{c} \sim 0.5$) in case 2. Left column: Late burning individual cycle, right column: Early burning individual cycle.

6.4 Model calibration constant α_{CFM}

Both lean and stoichiometric cases required an adjustment of the model constant α_{CFM} (Table 10) to fit to experimental data. For both lean cases, α_{CFM} is set to 0.4 while for the stoichiometric case we used $\alpha_{CFM} = 0.6$. Ideally, the same value should fit all cases. Several reasons could lead to this difference. The effect of decreasing α_{CFM} is to reduce the apparent heat release rate, thus the combustion speed.

Firstly, we cannot totally exclude an overestimation of the laminar flame speed estimated in lean condition at pressure and temperature representative of this engine. The experimental data used for the validation of the un-stretched laminar flame speeds (Section 11.2) are obtained at pressure, temperature and λ conditions much lower than the operating conditions under consideration (Table 14).

Another possible reason could be due to the combustion regime. In comparison to the stoichiometric conditions, at high enleanment the un-stretched laminar flame speed decreases significantly while the flame thickness increases (Table 14).

We define the Karlovitz number as the ratio of the flame time scale to the Kolmogorov scale.

$$Ka = t_F/t_\eta = \left(u'/S_L^0\right)^{3/2} \left(l_t/\delta_L\right)^{-1/2} \quad 25$$

l_t is the turbulent length scale, u' the turbulent intensity, S_L^0 the un-stretched laminar flame speed and δ_L the flame thickness.

Table 14

In-cylinder pressure, temperature and estimated laminar flame speed and flame thickness according to Section 11.2 for both stoichiometric and lean cases at spark timing.

Case	RPM	λ	Tu / K	P / bar	S_L^0 (cm/s)	δ_L / μm
1	1500	1	745	23	84.1	21.7
2, 3	1900	1.83	745	31	24.7	47.6

Considering that both engine configurations share similar geometry, we can assume that the integral length scale l_t is proportional to the combustion chamber typical dimension. As well, we assume that u' scales with the

crank angular velocity. As a result, the ratio of Karlovitz number between lean and stoichiometric conditions can be approximated as follows.

$$\frac{Ka_{lean}}{Ka_{stoich}} = \left(\frac{S_{L,stoich}^0 \cdot RPM_{lean}}{S_{L,lean}^0 \cdot RPM_{stoich}} \right)^{3/2} \left(\frac{\delta_{L,lean}}{\delta_{L,stoich}} \right)^{1/2} \approx 13.2$$

This suggests that the engine operates in lean conditions at Karlovitz number more than 1 order of magnitude higher than in stoichiometric conditions. This difference is significant considering that the ECFM-LES combustion model assumes a flamelet regime.

6.5 Validity of LES statistics

Both lean and stoichiometric cases' statistics have been evaluated over ten to twelve cycles (Table 9), the initialization cycles being discarded. Figure 25 and Figure 26 show the convergence of respectively the mean and the unbiased standard deviation of CA50 for the three LES cases. It appears clearly that more cycles would have been required to achieve better convergence, especially for case 1. Despite this consideration, we observed in section 6.1 that the trends are captured. For case 1 in particular, the mean burn rate and variability (Table 11) compare well to the experiment. Regarding the lean cases (case 2 and case 3), we cannot definitely ignore the effect of the indetermination of the spark plug orientation, which motivates the analysis of two extreme configurations. The case 2 aims at favoring a strong flow between electrodes while case 3, on the contrary, has been chosen so that the ground electrode protects the early flame kernel from the remaining tumble flow at spark timing (Figure 22). Despite the aforementioned uncertainty, the in-cylinder pressure envelope (Figure 14) and the burn rate variability (Figure 15 and Table 12) suggest that case 2 is reasonably representative.

The authors underline that this study has been realized based on an industrial complex geometry and a high mesh refinement [43], aiming at combining a well-defined LES, the modelling of physical phenomena and the industrial requirements. A set of 10 to 15 cycles could be sufficient to extract most combustion variability's characteristics, provided a monitoring of the convergence be done, some cases requiring more cycles. It is however expected that the extraction of low frequency outlier cycles and their subsequent analysis would require more cycles [55].

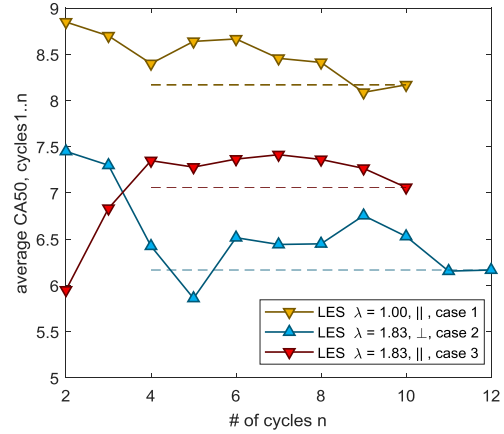


Figure 25
Mean CA50 for cycles' sets of increasing size. Orange triangles: LES case 1 (stoichiometric, || configuration); blue triangles, LES case 2 (lean, ⊥ configuration); red triangles, LES case 3 (lean, || configuration).

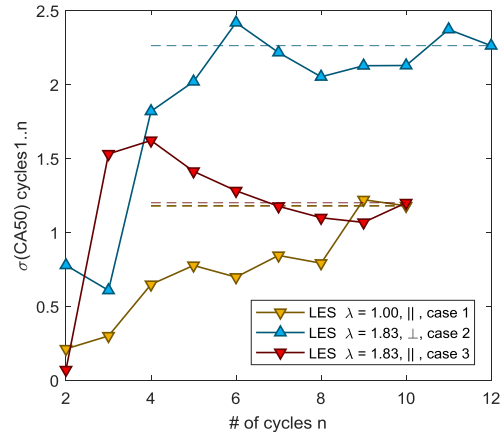


Figure 26
Unbiased standard deviation of CA50 for cycles' sets of increasing size. Orange triangles: LES case 1 (stoichiometric, || configuration); blue triangles, LES case 2 (lean, ⊥ configuration); red triangles, LES case 3 (lean, || configuration).

7 CONCLUSIONS

A modeling approach based on flame surface density and Large-Eddy Simulation has been developed and applied to the study of a concept lean burn engine permitting to explore the coupled effects of turbulence and flame propagation on the cycle-to-cycle combustion variabilities. The development was adapted from the CFM-LES model to account for the non-linear stretched effects on flame propagation occurring in such ultra-lean conditions and was validated on a complex engine configuration with direct injection and real spark-ignition systems by operating parametric variations from lean to stoichiometric conditions. In ultra-lean conditions, a strong reduction of the burning rate due to non-linear stretch effects during the early stage of the flame development was observed. The proposed model estimates this reduction up to a factor of three in ultra-lean conditions while there is almost no change for stoichiometric conditions. Moreover, only little change in the modeling parameters was necessary for covering these various turbulence/chemistry interactions regimes

(one order of magnitude difference for the Karlovitz number).

This investigation and validation work conducted on a research high-efficiency concept engine is a first step towards the understanding of the coupled mechanisms leading to unsteadiness of combustion in lean burn engine conditions. The fuel enrichment brings the combustion process to its low inflammability limit, which results in low laminar burning rates and imposes enhanced in-cylinder aerodynamics. This study has highlighted the required accuracy for describing the fuel burning intensities and the necessity to include new modeling features such as Markstein effects in such conditions. Additionally the spark-plug orientation effects on the combustion process was studied in details opening the way to engine design optimization in view of reducing CCV and thus to increase engine efficiency in a wider range of real operating conditions. It was demonstrated that the use of LES permits to capture turbulence/chemistry interactions in such complex situations and to get reliable results without much tuning of the modeling parameters. The present approach could be extended to account for other kinds of conditions such as dilution effects by exhaust gas recirculation for instance. Future work will permit to exploit the present modeling, simulation tools and methodologies as a whole to study new engine concepts and make appropriate choices to better control the reacting flow.

8 ACKNOWLEDGEMENTS

The authors would like to thank Fabrice Foucher from the University of Orléans for providing experimental data for laminar flame speed and Markstein length of iso-octane and to Liming Cai from Institut für Technische Verbrennung, RWTH Aachen University for providing the kinetic mechanism used in CHEM1D calculations. Lastly, we would like to thank Pawel Luszcz for his substantial contribution to the lean burn combustion project at TGR-E.

9 CONFLICT OF INTEREST:

The authors declare that they have no conflict of interest.

10 BIBLIOGRAPHY

- [1] Kalghatgi G., Levinsky H., Colket M.: Future transportation fuels. *Prog. in Energy and Combust. Sci.* 69, 103-105 (2018). <https://doi.org/10.1016/j.pecs.2018.06.003>.
- [2] Fontanesi, S., Paltrinieri, S., D'Adamo, A., Cantore, G.: Knock Tendency Prediction in a High Performance Engine Using LES and Tabulated Chemistry. *SAE Int. J. Fuels Lubr.* 6, 98-118 (2013). <https://doi.org/10.4271/2013-01-1082>.
- [3] Misdariis A, Vermorel O. Poinso T.: LES of knocking in engines using dual heat transfer and two-step reduced schemes. *Combust. and Flame*, 162, 4304 – 4312, (2015). <https://doi.org/10.1016/j.combustflame.2015.07.023>.
- [4] Robert A, Richard S., Colin O., Martinez L., De Francqueville L. LES prediction and analysis of knocking combustion in a spark ignition engine. *Proc. of the Combust. Inst.*, 35, 2941-2948, (2015). <https://doi.org/10.1016/j.proci.2014.05.154>.
- [5] Koch J., Schmitt M., Wright Y.M., Steurs K., Boulouchos K. LES multi-cycle analysis of the combustion process in a small SI engine. *SAE Int. J. Engines* 7, 269-285, (2014). <https://doi.org/10.4271/2014-01-1138>.
- [6] Ameen M.M., Mirzaeian M., Millo F., Som S. Numerical prediction of cyclic variability in a spark ignition engine using a parallel large eddy simulation approach. *J. Energy Res. Technol.*, 140, (2018). <https://doi.org/10.1115/1.4039549>.
- [7] Truffin K., Angelberger C., Richard S., Pera C. Using large eddy simulation and multivariate analysis to understand the sources of combustion cyclic variability in a spark ignition engine. *Combust. and Flame*, 162, 4371-4390, (2015). <https://doi.org/10.1016/j.combustflame.2015.07.003>.
- [8] Rutland, C. J. Large-eddy simulations for internal combustion engines – a review. *Int. J. Engine Res.*, 12, 421–451, (2017). <https://doi.org/10.1177/146808741407248>.
- [9] Falkenstein T., Kang S., Davidovic, M., Bode M., Pitsch H., Kamatsuchi T. et al. LES of Internal Combustion Engine Flows Using Cartesian Overset Grids. *Oil & Gas Sci. and Technol.*, 72, (2017). <https://doi.org/10.2516/ogst/2017026>.
- [10] Janas P., Wlokas I., B., Böhm and A., Kempf. On the Evolution of the Flow Field in a Spark Ignition Engine. *Flow, Turb. and Combust.*, 98, 237–264, (2017). <https://doi.org/10.1007/s10494-016-9744-3>.
- [11] Chen C., Ameen M. M., Wei H., Iyer C., Ting F., Vanderwege B., Som B. LES Analysis on Cycle-to-Cycle Variation of Combustion Process in a DISI Engine. *International Powertrains. SAE Technical Paper 2019-01-0006*, (2019). <https://doi.org/10.4271/2019-01-0006>.
- [12] Falkenstein T., Kang S., Pitsch H. Analysis of premixed flame kernel/turbulence interactions under engine conditions based on direct numerical simulation data. *J. of Fluid Mech.*, 885, (2020). <https://doi.org/10.1017/jfm.2019.995>.
- [13] Ghaderi Masouleh M., Keskinen K., Kaario O., Kahila H., Karimkashi S., Vuorinen V. Modeling cycle-to-cycle variations in spark ignited combustion engines by scale-resolving simulations for different engine speeds. *Appl. Energy*, 250, 801-820, (2019). <https://doi.org/10.1016/j.apenergy.2019.03.198>.
- [14] Wadekar S., Janas P., Oevermann M. Large-eddy simulation study of combustion cyclic variation in a lean-burn spark ignition engine. *Appl. Energy*, 255, (2019). <https://doi.org/10.1016/j.apenergy.2019.113812>.
- [15] Richard S., Colin O., Vermorel O., Benkenida A., Angelberger C., Veynante D. Towards large eddy simulation of combustion in spark ignition engines. *Proc. Combust. Inst.*, 31, 3059 - 3066, (2007). <https://doi.org/10.1016/j.proci.2006.07.086>.
- [16] Fontanesi S., d'Adamo A., Rutland C J. Large-Eddy simulation analysis of spark configuration effect on cycle-to-cycle variability of combustion and knock. *International J. of Engine Res.*, (2015). <https://doi.org/10.1177/1468087414566253>.
- [17] Nicoud F., Baya Toda H., Cabrit O., Bose S., Lee J. Using singular values to build a subgrid-scale model for Large-Eddy Simulations. *Physics of Fluids*, 23, (2011). <https://doi.org/10.1063/1.3623274>.
- [18] Vermorel O., Richard S., Colin O., Angelberger C., Benkenida A., Veynante D. Towards the understanding of cyclic variability in a spark ignited engine using multi-cycle LES. *Combust. and Flame*, 156, Issue 8, 1525-1541, (2009). <https://doi.org/10.1016/j.combustflame.2009.04.007>.
- [19] Richard, S., Colin, O., Vermorel, O., Benkenida, A., Veynante, D. Development of LES models based on the flame surface density approach for ignition and combustion in SI engines. *ECCOMAS Thematic Conference on computational combustion*, 1 - 20, (2005).
- [20] Colin O., Ducros F., Veynante D., Poinso T. A thickened flame model for large eddy simulations of turbulent premixed combustion. *Physics of Fluids*, 12, (2000). <https://doi.org/10.1063/1.870436>.

- [21] Bougrine S., Richard S., Colin O., Veynante D. Fuel Composition Effects on Flame Stretch in Turbulent Premixed Combustion: Numerical Analysis of Flame-Vortex Interaction and Formulation of a New Efficiency Function. *Flow Turb. and Combust.*, (2014). 93, 259–281, <https://doi.org/10.1007/s10494-014-9546-4>.
- [22] Colin O., Truffin K. A spark ignition model for large eddy simulation. *Proc. of the Combust. Inst.*, 33, 3097–3104, (2011). <https://doi.org/10.1016/j.proci.2010.07.023>.
- [23] Colin O., Duclos J.M. Arc and kernel tracking ignition model for 3D spark-ignition engine calculations. *The Proc. of the Int. symp. on diagn. and modeling. of combust. in intern. combust. engines*, 343-350, (2001). <https://doi.org/10.1299/jmsesdm.01.204.46>.
- [24] Galmiche B., Halter F., Foucher F. Effects of high pressure, high temperature and dilution on laminar burning velocities and Markstein lengths of iso-octane/air mixtures. *Combust. and Flame*, 159, 3286–3299, (2012). <https://doi.org/10.1016/j.combustflame.2012.06.008>.
- [25] Bonhomme A., Selle L., Poinso T. Curvature and confinement effects for flamespeed measurements. *Combust. and Flame*, 160, 1208–1214, (2013). <https://doi.org/10.1016/j.combustflame.2013.02.003>.
- [26] Weiss M., Zarzalis N., Suntz R. Experimental study of Markstein number effects on laminar flamelet velocity in turbulent premixed flames. *Combust. and Flame*, 154, 671-691, (2008). <https://doi.org/10.1016/J.COMBUSTFLAME.2008.06.011>.
- [27] Bray K. N. C., Cant R. S. Some applications of Kolmogorov's turbulence research in the field of combustion. *Proc. of the Royal Society A*, 434, Issue 1890, (1991). <https://doi.org/10.1098/rspa.1991.0090>.
- [28] Tabor G., Weller H.G. Large-Eddy Simulation of Premixed Turbulent Combustion Using Flame Surface Wrinkling Model. *Flow, Turb. and Combust.*, 72, (2004). <https://doi.org/10.1023/B:APPL.0000014910.06345.fb>.
- [29] Weller H.G., Tabor G., Gosman A.D., Fureby C. Application of a flame-wrinkling LES combustion model to a turbulent mixing layer. *Symposium (Int.) on Combustion*, 27, 899-907, (1998). [https://doi.org/10.1016/S0082-0784\(98\)80487-6](https://doi.org/10.1016/S0082-0784(98)80487-6).
- [30] Clavin P., Williams F. Effects of molecular diffusion and of thermal expansion on the structure and dynamics of premixed flames in turbulent flows of large scale and low intensity. *J. of Fluid Mechanics*, 116, 251-282, (1982). <https://doi.org/10.1017/S0022112082000457>.
- [31] Im, H. G., Chen, J. H. Effects of flow transients on the burning velocity of laminar hydrogen/air premixed flames. *Proc. of the Combustion Inst.*, 28, 1833-1840, (2000). [https://doi.org/10.1016/S0082-0784\(00\)80586-X](https://doi.org/10.1016/S0082-0784(00)80586-X).
- [32] Curran H.J., Gaffuri P., Pitz W.J., Westbrook C.K. Oxidation, A comprehensive modeling study of iso-octane. *Comb. and Flame*, 129, 253-280, (2002). [https://doi.org/10.1016/S0010-2180\(01\)00373-X](https://doi.org/10.1016/S0010-2180(01)00373-X).
- [33] Mehl M., Curran H. J., Pitz W. J., Westbrook C. K. Chemical kinetic modeling of component mixtures relevant to gasoline. *4th Eur. Combust. Meet., Vienna, Austria*, (2009).
- [34] Mehl M., Pitz W. J., Sjöberg M., Dec J. E. Detailed kinetic modeling of low-temperature heat release for PRF fuels in an HCCI engine. *SAE Technical Paper 2009-01-1806*, (2009). <https://doi.org/10.4271/2009-01-1806>.
- [35] Cai L., Pitsch H. Optimized chemical mechanism for combustion of gasoline surrogate fuels. *Combust. and Flame*, 162, 1623-1637, (2015). <https://doi.org/10.1016/j.combustflame.2014.11.018>.
- [36] Cai L., Ramalingam A., Minwegen H., Alexander Heufer K., Pitsch H. Impact of exhaust gas recirculation on ignition delay times of gasoline fuel: An experimental and modeling study. *Proc. of the Combust. Inst.*, 37, 639-647, (2019). <https://doi.org/10.1016/j.proci.2018.05.032>.
- [37] Kee R. J., Coltrin M. E., Glarborg P., Zhu H. *Chemically Reacting Flow: Theory, Modeling, and Simulation*, 2nd Edition. John Wiley and Sons, (2017).
- [38] Goodwin D. G., Speth R. L., Moffat H. K., Weber B. W. *Cantera: An object-oriented software toolkit for chemical kinetics, thermodynamics, and transport processes*. <https://www.cantera.org>, (2018).
- [39] Groot G. R. A., De Goey L. P. H. A computational study on propagating spherical and cylindrical premixed flames. *Proc. of the Combust. Inst.*, 29, 1445-1451, (2002). [https://doi.org/10.1016/S1540-7489\(02\)80177-8](https://doi.org/10.1016/S1540-7489(02)80177-8).
- [40] Groot G. R. A., Modelling of propagating spherical and cylindrical premixed flames. *Technische Universiteit Eindhoven*, PhD Thesis, (2003). <https://doi.org/10.6100/IR570155>.
- [41] de Goey L.P.H., van Oijen J.A., Hermanns R.T.E., and Bongers H. *CHEM1D: a package for the simulation of one-dimensional flames*. *Technische Universiteit Eindhoven*, (2003).
- [42] Luszcz P., Takeuchi K., Pfeilmaier P., Gerhardt M., Adomeit P., Brunn A., Kupiek C., Franzke B. Homogeneous Lean Burn Engine Combustion System Development – Concept study. In. *18. Internationales Stuttgarter Symposium. Proceedings. Springer Vieweg, Wiesbaden*, 205-223, (2018). https://doi.org/10.1007/978-3-658-21194-3_19.
- [43] Benoit O., Luszcz P., Drouvin Y., Kayashima T., Adomeit P., Brunn A., Jay S., Truffin K., Angelberger C. Study of Ignition Processes of a Lean Burn Engine Using Large-Eddy Simulation. *SAE Technical Paper 2019-01-2209*, (2019). <https://doi.org/10.4271/2019-01-2209>.
- [44] Lax P.D., Wendroff B. *Systems of Conservation Laws, Communications on Pure and Applied Mathematics*. *Communications on Pure and Appl. Mathematics*, 13, 217-237, (1960). <https://doi.org/10.1002/cpa.3160130205>.
- [45] Moureau V., Lartigue G., Sommerer Y., Angelberger C., Colin O., Poinso T. Numerical methods for unsteady compressible multi-component reacting flows on fixed and moving grids. *J. of Comput. Physics*, 202, 710-736, (2005). <https://doi.org/10.1016/j.jcp.2004.08.003>.
- [46] Reveille B., Gillet N., Bohbot J., Laget O. Automatic Body-Fitted Hybrid mesh generation for Internal Combustion Engine Simulations. *SAE Technical Paper 2014-01-1133*, (2014). <https://doi.org/10.4271/2014-01-1133>.
- [47] Poinso T.J., Lele S.K. Boundary Conditions for Direct Simulations of Compressible Viscous Flows. *J. of Computational Physics*, 101, 104-129, (1992). [https://doi.org/10.1016/0021-9991\(92\)90046-2](https://doi.org/10.1016/0021-9991(92)90046-2).
- [48] Nicoud E., Quantifying combustion robustness in GDI engines by Large-Eddy Simulation. *PhD Thesis, Université Paris-Saclay, Saint-Aubin, France*, 45-59. (2018).
- [49] Nicoud E., Colin O., Angelberger C., Krüger C., Nicollet F. A no-slip wall law formulation for cell-vertex codes, validated for LES of internal aerodynamics. In *LES4ICE Conference 2016, IFPEN, Reuil-Malmaison*, (2016).
- [50] Garcia M., Riber E., Simonin O., Poinso T. Comparison between Euler/Euler and Euler/Lagrange LES approaches for confined bluff-body gas-solid flow prediction. In *International Conference on Multiphase Flow*, (2007).
- [51] Habchi C., The energy spectrum analogy breakup (SAB) model for the numerical simulation of sprays. *Atomization and Sprays*, 21, 1033–1057, (2011). <https://doi.org/10.1615/AtomizSpr.2012004531>.
- [52] Abramzon B., Sirignano W. A. Droplet vaporisation model for spray combustion calculations. *Int. J. Heat and Mass Transfer*, 1605–1618, (1989). [https://doi.org/10.1016/0017-9310\(89\)90043-4](https://doi.org/10.1016/0017-9310(89)90043-4).
- [53] Pope S. B. Ten questions concerning the large-eddy simulation of turbulent flows. *New J. of Physics*, 6, (2004). <https://doi.org/10.1088/1367-2630/6/1/035>.
- [54] Nguyen T., Kempf A. M. Investigation of Numerical Effects on the Flow and Combustion in LES of ICE. *Oil & Gas Sci. and Technol. – Rev. IFP Energies nouvelles*, 72 (4), (2017). <https://doi.org/10.2516/ogst/2017023>.
- [55] Krüger Ch., Schorr J., Nicollet F., Bode J., Dreizler A., Böhm B. Cause-and-effect chain from flow and spray to

heat release during lean gasoline combustion operation using conditional statistics. *Int. J. of Engine Res.*, 18, 1-2, (2017). <https://doi.org/10.1177/1468087416686721>.

- [56] Endouard C., Halter F., Chauveau C., Foucher F. Effects of CO₂, H₂O, and Exhaust Gas Recirculation Dilution on Laminar Burning Velocities and Markstein Lengths of

Iso-Octane/Air Mixtures. *Combust. Science and Tech.*, (2016). 516-528, <https://doi.org/10.1080/00102202.2016.1138792>.

11 APPENDIX

11.1 Un-stretched laminar flame speed governing equations

Continuity equation:

$$\frac{\partial(\rho u)}{\partial z} = 0$$

Species' transport:

$$\rho u \frac{\partial Y_K}{\partial z} = -\frac{\partial j_k}{\partial z} + \dot{\omega}_k$$

Energy equation:

$$\rho u c_p \frac{\partial T}{\partial z} = \frac{\partial}{\partial z} \left(\lambda \frac{\partial T}{\partial z} \right) - \left(\sum_k c_{p,k} j_k \right) \frac{\partial T}{\partial z} - \sum_k h_k W_k \dot{\omega}_k$$

The state variables ρ , u , T and c_p represent respectively the mixture density, the axial velocity, the system temperature and the heat capacity at constant pressure.

Y_K , $c_{p,k}$, h_k , W_k , $\dot{\omega}_k$ are respectively the mass fraction, the specific heat capacity, the enthalpy, the molecular weight and the molar production rate of species k .

The diffusive mass flux j_k is evaluated using the multicomponent formulation

$$j_k = \frac{\rho W_k}{\bar{W}^2} \sum_i W_i D_{k,i} \frac{\partial X_i}{\partial z} - \frac{D_k^T}{T} \frac{\partial T}{\partial z}$$

where $D_{k,i}$ is the multicomponent diffusion coefficient and D_k^T is the Soret diffusion coefficient.

11.2 Un-stretched Flamelet Calculation Validation

Our calculations have been validated against experimental results of spherical expanding flame in a constant volume vessel obtained in [24], at 1, 2, 5 10 bar for the pressure and 323K 373K, 423K, 473K for the temperature. The fuel-air equivalence ratio was also varied over the maximal admissible range during the experiment.

Figure 27 illustrates the correlation between calculated un-stretched laminar flame speed and experiment for all considered conditions. The discrepancy is less than 5% in most cases. Figure 28 compares the un-stretched laminar flame speed as a function of ϕ for both calculation and experiment. The correlation is good at 2 and 5 bar and fair at 1 bar and 10 bar.

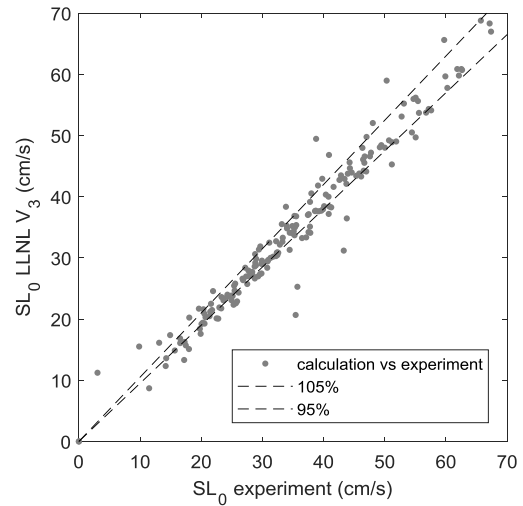
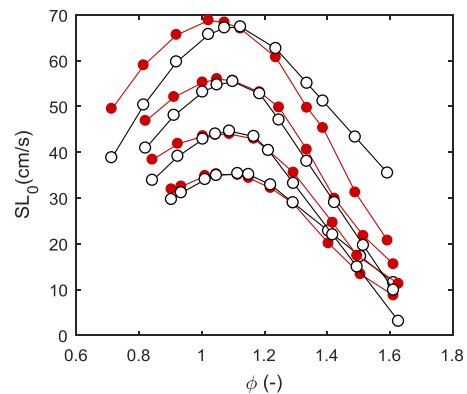
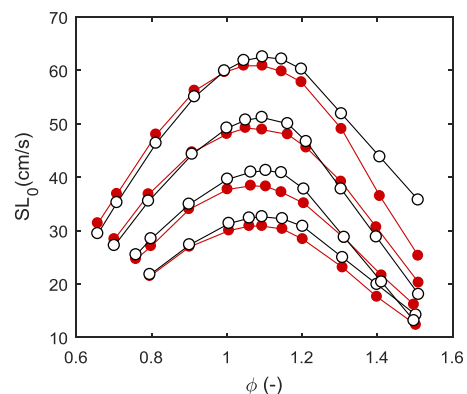


Figure 27
Correlation graph simulation versus experiment for the un-stretched laminar flame speed.



1 bar



2 bar

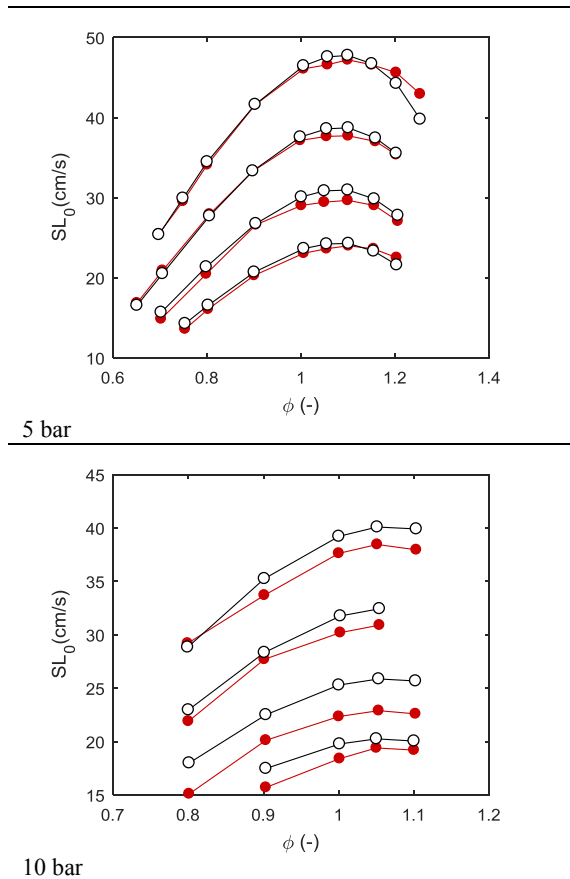


Figure 28
Comparison between calculated laminar flame speeds and experimental results at 1, 2, 5 and 10 bar. Red: experiment, black: calculation. $T=323\text{K}$ (lowest curve), 373K , 423K , 473K (highest curve)

11.3 Cycle-to-cycle correlation analysis of experimental data

Figure 29 and 30 show respectively the cycle-to-cycle correlation of CA50 and CA10-75 for the lean burn experimental case.

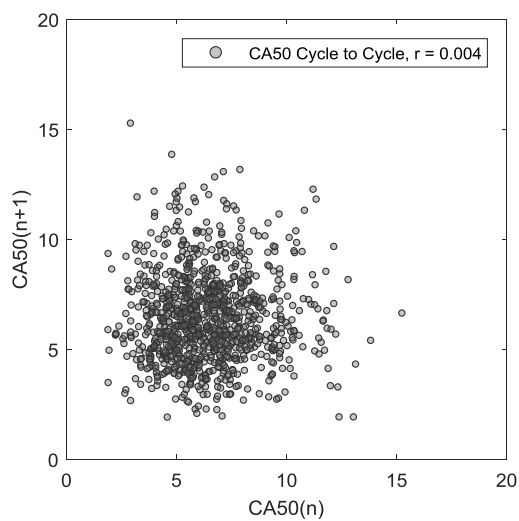


Figure 29

Case 2: Cycle-to-cycle correlation of CA50, $\lambda=1.83$, Experimental data

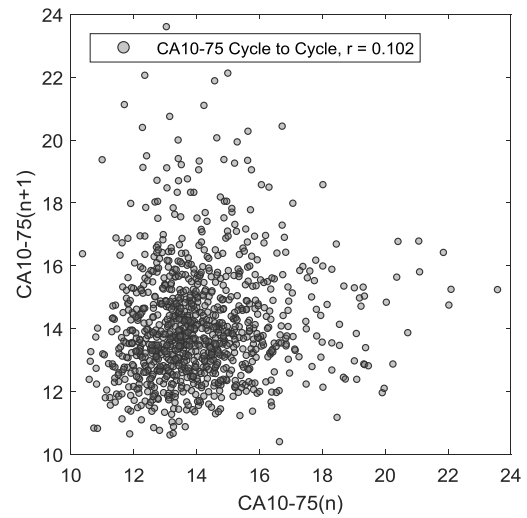


Figure 30
Case 2: Cycle-to-cycle correlation of CA10-75, $\lambda=1.83$, Experimental data

11.4 Effect of stretch in stoichiometric condition

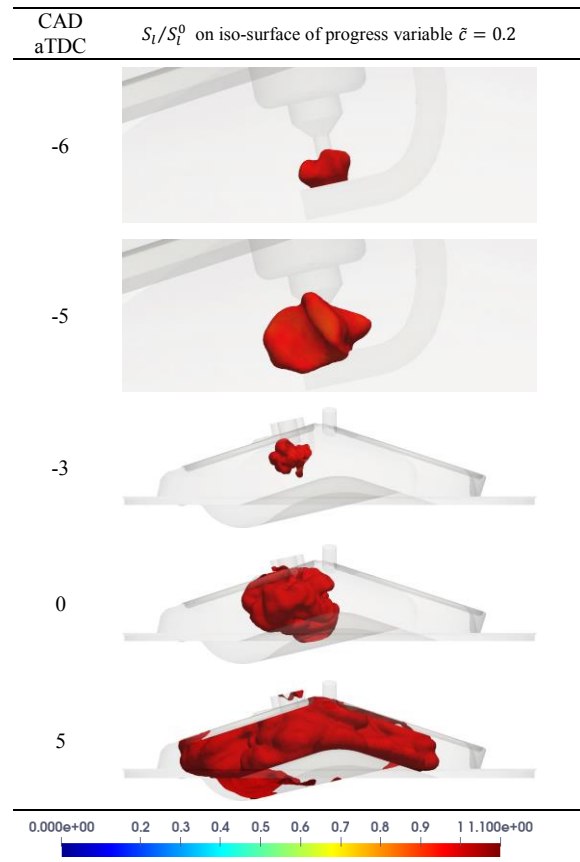


Figure 31
Case 1, evolution of flame propagation represented by Iso-surface of progress variable $\tilde{c} = 0.2$, colored by S_t/S_t^0

